

1 **Integrative network toxicology reveals lipoprotein lipase as a key mediator of dibutyl**
2 **phthalate-associated head and neck squamous cell carcinoma**

3 Guangming Li ^{a 1}, Yi Jin ^{c 1}, Xiaowei Yuan ^b, Xinyan Wu ^f, Long Li ^g, Jiashu Liao ^{d e},

4 Shanshan Cai ^a

5 ^aDivision of Biomedical and Life Sciences, Faculty of Health and Medicine, Lancaster
6 University, Lancaster, LA1 4YG, United Kingdom

7 ^bDepartment of Surgery, Xi'an Xincheng Huaqing Hospital, Xi'an, 710032, China

8 ^cSchool of Cellular and Molecular Medicine, University of Bristol, Bristol, BS8 1QU, United
9 Kingdom

10 ^dUniversity of Glasgow, School of Computer Science, Glasgow, G12 8QQ, United Kingdom

11 ^eSchool of Computer Science, University of Leeds, Leeds, LS2 9JT, United Kingdom

12 ^fCollege of Food Science and Nutritional Engineering, China Agricultural University, Beijing,
13 100083, China

14 ^gNutrition and Dietetic Services, Gloucestershire Royal Hospital, NHS Foundation Trust,
15 National Health Service(NHS), Gloucester, GL1 3NN, United Kingdom

16

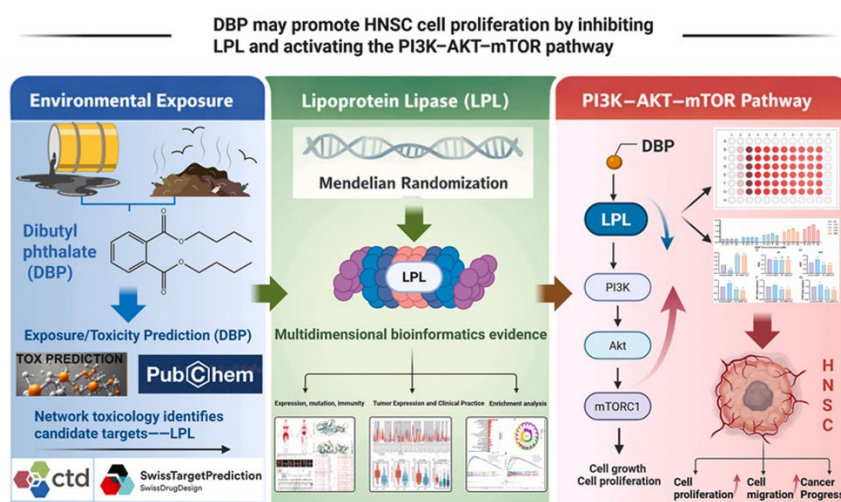
17 **Abstract**

18 Dibutyl phthalate (DBP) is a widely distributed endocrine-disrupting chemical with potential
19 carcinogenic properties, yet its role in head and neck squamous cell carcinoma (HNSC) remains
20 unclear. Here, we applied an integrative framework combining network toxicology, Mendelian
21 randomization (MR), multi-omics analyses, molecular docking, molecular dynamics
22 simulations, and in vitro experiments to elucidate the mechanisms underlying DBP-associated
23 HNSC. Lipoprotein lipase (LPL) was identified as the sole overlapping gene between DBP-
24 related targets and HNSC-associated genes. MR analysis supported a potential causal
25 relationship between LPL and HNSC susceptibility. Expression profiling demonstrated tissue-

26 and cell type-specific patterns of LPL and its dysregulation in HNSC, with associations to
27 tumor stage and prognosis. Genomic analyses revealed that LPL alterations were infrequent
28 and mainly driven by copy number loss. LPL expression positively correlated with immune and
29 stromal infiltration. Enrichment analyses implicated immune regulation and PI3K-AKT
30 signaling. Molecular simulations showed stable DBP-LPL binding. Functionally, DBP
31 promoted SCC9 proliferation and reduced LPL expression, and was associated with
32 transcriptional changes in PI3K-AKT-mTOR-related genes, whereas LPL restoration
33 mitigated these effects. These findings reveal a novel DBP-LPL axis in HNSC.

34

35 Graphical abstract



36

37

38 **Keywords:** Dibutyl phthalateHead and neck squamous cell carcinoma; Lipoprotein lipase;
39 Network toxicology

40

41 1. Introduction

42 Dibutyl phthalate (DBP) is a commonly used plasticizer extensively employed in plastic
43 products, cosmetics, and coatings, leading to its widespread presence in the environment
44 (Silano et al., 2019; Lv et al., 2025). As a typical environmental endocrine-disrupting chemical,
45 DBP has not been formally classified as a human carcinogen; however, animal studies have

46 demonstrated its ability to induce gene mutations, suggesting potential carcinogenic risk (Xiang
47 et al., 2025; Pan et al., 2024). Following accumulation in the body, DBP and related phthalates
48 can disrupt endocrine function and cause toxic damage to various tissues and organs, such as
49 the liver, kidneys, and reproductive system (Li et al., 2024; Arrigo et al., 2023).
50 Epidemiological studies have also indicated that human exposure to phthalates through multiple
51 pathways, including dietary intake and inhalation, may increase the risk of cancer (Yu and Wang,
52 2022; Meng et al., 2024). Nevertheless, research on the role of DBP in the development and
53 progression of specific tumors, such as head and neck squamous cell carcinoma (HNSC),
54 remains relatively scarce.

55 Head and neck squamous cell carcinoma (HNSC) is a malignant tumor originating from the
56 mucosal epithelium of sites such as the oral cavity and pharynx (Johnson et al., 2020; Liu et al.,
57 2024). Its occurrence rate remains high globally, with over 850,000 new cases and
58 approximately 440,000 related deaths annually (Barsouk et al., 2023; Gormley et al., 2022).
59 High-risk factors for HNSC include smoking, alcohol abuse, and high-risk human
60 papillomavirus (HPV) infection, but exposure to environmental carcinogens is also considered
61 a potential contributing factor (Barsouk et al., 2023; Báez A, 2008). Despite recent
62 advancements in treatment modalities, including surgery, radiotherapy, chemotherapy, and
63 immunotherapy, the prognosis for patients with advanced HNSC remains poor, with a 5-year
64 survival rate of only about 40% for stage III–IV patients (Park et al., 2021). This situation
65 underscores the need to investigate the environmental factors and molecular mechanisms
66 underlying HNSC development, aiming to provide new insights for prevention and treatment.
67 Notably, the mechanisms by which endocrine-disrupting chemicals, such as DBP and other
68 environmental pollutants, contribute to head and neck tumors remain unclear, and this research
69 gap constitutes a key starting point for the present study.

70 From a broader oncological perspective, tumor initiation and progression arise from the
71 accumulation of genetic and epigenetic alterations in the context of environmental exposures,
72 together driving complex and heterogeneous disease phenotypes. Cancer development is not
73 solely governed by intrinsic genomic events but is also profoundly shaped by external factors,
74 including environmental carcinogens, which can influence both cellular metabolism and the

75 tumor microenvironment. In parallel, advances in cancer biology have driven a major shift in
76 therapeutic paradigms—from conventional cytotoxic approaches toward molecularly targeted
77 therapies and immunomodulatory strategies—highlighting the importance of understanding
78 context-specific molecular mechanisms that underlie tumor progression and treatment response
79 (Sonkin et al., 2024). Recent integrative multi-omics analyses have further revealed that
80 tumorigenesis is orchestrated through coordinated interactions among diverse molecular layers,
81 including genomic, transcriptomic, and metabolic networks. In this framework, metabolic
82 genes are increasingly recognized not merely as downstream effectors but as critical regulatory
83 intermediates that interface with canonical oncogenic signaling pathways and contribute to key
84 hallmarks of cancer, such as proliferative signaling, metabolic reprogramming, and immune
85 evasion (Ubaid et al., 2025). These insights suggest that environmentally responsive metabolic
86 regulators may act as pivotal nodes linking external exposures to intracellular signaling and
87 phenotypic outcomes. In this context, investigating metabolic genes that are responsive to
88 environmental toxicants, such as LPL, may provide important mechanistic insights into how
89 environmental exposures contribute to tumor development and progression, and may help
90 identify potential targets for therapeutic intervention.

91 Tumorigenesis is often accompanied by metabolic reprogramming and immune dysregulation
92 within the tumor microenvironment, with abnormalities in lipid metabolism being particularly
93 prominent (Jin et al., 2023; Yang et al., 2023). Lipoprotein lipase (LPL) is a key enzyme in
94 systemic lipid metabolism, responsible for hydrolyzing triglycerides in circulating lipoproteins
95 to release fatty acids (Borén et al., 2022; Kersten, 2014). In the context of tumor metabolism,
96 studies have demonstrated that certain tumor cells can utilize LPL to acquire exogenous fatty
97 acids to promote their own proliferation; inhibiting LPL activity impairs the growth capacity of
98 tumor cells (Zaidi et al., 2013; Xiao et al., 2024). On the other hand, LPL is also involved in
99 regulating the tumor immune microenvironment: recent reports have shown that upregulating
100 LPL expression can inhibit tumor cell proliferation and promote the polarization of
101 macrophages toward the anti-tumor M1 phenotype, enhancing immune cell infiltration into
102 tumors, thereby significantly suppressing tumor progression in breast cancer models (Yang et
103 al., 2025; Oliviero et al., 2025). This suggests that LPL may play a dual role in tumor biology,

104 being associated with both tumor energy supply and metabolic reprogramming, as well as
105 influencing anti-tumor immune responses. However, the function of LPL in head and neck
106 squamous cell carcinoma (HNSC) has not been fully investigated, and there is a particular lack
107 of information regarding the impact of the environmental toxicant dibutyl phthalate (DBP) on
108 LPL expression and function.

109 Based on a network toxicology strategy that integrates environmental toxicants with disease
110 molecular networks, this study aims to elucidate the potential carcinogenic mechanisms of DBP
111 in HNSC, with a focus on the role of LPL. Data from public databases (e.g., TCGA, GEO) were
112 integrated to analyze the differential expression of LPL in HNSC tissues and its association
113 with patient survival, and to predict and validate whether LPL may act as a protective factor in
114 DBP-related carcinogenesis. Furthermore, molecular docking and molecular dynamics
115 simulations were employed to assess the binding capability between DBP and the LPL protein.
116 At the cellular level, qPCR and CCK-8 assays were used to detect the effects of DBP treatment
117 on LPL gene expression and cell viability in HNSC cells, respectively. Through these
118 investigations, we aim to untangle the molecular pathways through which DBP promotes the
119 development and progression of HNSC and the regulatory role of LPL therein, providing new
120 insights and potential intervention targets for mechanistic studies on environmental
121 carcinogenesis in head and neck tumors.

122

123 **2. Materials and methods**

124 **2.1. Network toxicology analysis**

125 **2.1.1. Network-based target identification for DBP**

126 The three-dimensional chemical structure of di-*n*-butyl phthalate (DBP) was retrieved from the
127 PubChem database (<https://pubchem.ncbi.nlm.nih.gov/compound/3026>) (Kim et al.,
128 2023; Kim, 2019; Wang et al., 2012). Toxicological properties, including predicted oral
129 LD₅₀ values and key physicochemical parameters, were obtained through the ProTox-II
130 prediction platform (https://tox.charite.de/protox_II), which also provided functional
131 annotations such as toxicity classification and predicted bioactivity.

132 To comprehensively characterize the potential biological targets of DBP, we aggregated
133 compound–gene interaction data from three independent resources: the Comparative
134 Toxicogenomics Database (CTD, <https://ctdbase.org/>) (Mattingly et al., 2006; Davis et al.,
135 2009, 2023), STITCH, and SwissTargetPrediction. The datasets were curated and standardized
136 to generate a unified interaction network, serving as the foundation for downstream network
137 toxicology and enrichment analyses.

138 **2.2. Mendelian randomization analysis of druggable targets in HNSC**

139 To explore putative causal relationships between DBP-related targets and head and neck
140 squamous cell carcinoma (HNSC), we performed Mendelian randomization (MR) analysis
141 focusing on druggable genes. Candidate genes were intersected with entries from the Drug–
142 Gene Interaction Database (DGIdb, version 4.2.0, <https://www.dgiddb.org/>) (Cannon et al., 2024)
143 and curated druggable gene datasets reported by Finan et al. The lipoprotein lipase (LPL) gene,
144 identified as a shared target between DBP and HNSC, was prioritized for causal inference.

145 *Cis*-acting protein quantitative trait loci (*cis*-pQTLs) from human plasma proteomic data were
146 used as instrumental variables. Summary-level genetic association data for HNSC were
147 acquired from publicly available genome-wide association studies. MR analyses were
148 conducted using the TwoSampleMR package (version 0.6.2) in R, selecting independent
149 variants ($r^2 < 0.001$) to avoid confounding due to linkage disequilibrium. The inverse variance
150 weighted (IVW) method was applied as the primary estimator of causality, and sensitivity
151 analyses, including MR-Egger regression, MR-PRESSO, and leave-one-out testing, were
152 performed to validate the robustness of the findings.

153 Causal effect estimates were reported as beta coefficients or odds ratios (ORs), together with
154 their 95% confidence intervals (95% CIs) and corresponding exact *P* values. The primary MR
155 analysis was conducted using the inverse-variance weighted (IVW) method, and
156 complementary sensitivity analyses were performed using additional MR methods where
157 applicable. For correlation analyses, correlation coefficients were presented together with their
158 95% confidence intervals and exact *P* values. Pearson's correlation analysis was used for
159 normally distributed variables, while Spearman's rank correlation analysis was applied for non-

160 normally distributed data.

161 **3. Gene expression analysis of LPL**

162 To comprehensively characterize the expression profile of LPL in normal human tissues, we
163 retrieved and analyzed transcriptomic data from the Human Protein Atlas (HPA) database
164 (<https://www.proteinatlas.org/>) (Uhlén et al., 2017; Berglund et al., 2008). We systematically
165 analyzed tissue, single-cell, and subcellular modules, evaluating tissue-specific expression
166 patterns, single-cell RNA sequencing (scRNA-seq) profiles, and immunofluorescence-based
167 subcellular localization, respectively. To further elucidate the cell type distribution of LPL in
168 head and neck-related tissues (such as the tongue and salivary glands), we obtained and
169 analyzed the gingival scRNA-seq dataset from the DISCO Human Single Cell Omics Database
170 (<https://www.immunesinglecell.org/>) (Li et al., 2022, 2025). Furthermore, we assessed and
171 visualized the evolutionary conservation of LPL across vertebrate species using the UCSC
172 Cancer Genome Explorer (<https://genome-cancer.ucsc.edu/>) (CNCB-NGDC Members and
173 Partners, 2022; CNCB-NGDC Members and Partners, 2024; CNCB-NGDC Members and
174 Partners, 2025).

175 **4. Expression of LPL in HNSC and its clinical relevance**

176 Given the potential impact of gene expression on patients' clinical status, we performed clinical
177 correlation analyses using the TIMER2.0 database (<http://timer.cistrome.org/>) (Li et al.,
178 2016, 2020) and the BEST database (<https://rookieutopia.hiplot.com.cn/>).

179 **5. Genetic mutation analysis of LPL**

180 Using the cBioPortal for Cancer Genomics platform (<https://www.cbioportal.org/>) (Cerami et
181 al., 2012; Gao et al., 2013; de Bruijn et al., 2023), we analyzed LPL genomic alterations in head
182 and neck squamous cell carcinoma (HNSC) based on the TCGA Combined Study dataset. The
183 Cancer Types Summary and OncoPrint modules were used to characterize the mutation
184 spectrum and copy number alterations (CNAs) of LPL, including amplification, gain, shallow
185 deletion, and deep deletion, across TCGA tumor types. Alteration frequencies and mutation
186 counts were further compared among different cancer types and histological subgroups. In
187 addition, the TIMER3.0 database was employed to assess the association between LPL CNA

188 status and immune cell infiltration in HNSC, enabling an integrated evaluation of the genomic
189 alteration landscape of LPL and its potential immunological relevance.

190 **6. Structural and mutation site analysis**

191 We retrieved somatic mutation data of LPL from 496 patients with head and neck squamous
192 cell carcinoma (HNSC) in the TCGA PanCancer Atlas cohort using the cBioPortal database
193 (<https://www.cbioportal.org/>). The crystal structure of human LPL was obtained from the
194 Protein Data Bank (PDB: 6E7K) (<https://www.rcsb.org/>) (Berman et al., 2000). Three mutant
195 LPL protein structures were predicted using AlphaFold3
196 (<https://alphafoldserver.com/>). All protein structures were visualized using PyMOL, where
197 protein domains and mutation sites were annotated. Structural alignment between mutant and
198 wild-type LPL proteins was performed using the align command in PyMOL, and the root mean
199 square deviation (RMSD) of C α atoms was calculated to evaluate structural differences.
200 Residues within 4 Å of each mutated amino acid were displayed, and hydrogen bonds formed
201 with the mutated residues were identified and annotated.

202 **7. Immune infiltration analysis**

203 Using the TIMER3.0 platform (<https://compbio.cn/timer3/>) (Cui et al., 2025; Li et al., 2017),
204 we systematically analyzed the association between LPL expression and immune cell
205 infiltration across multiple tumor types. Partial correlation analyses were performed to evaluate
206 the relationships between LPL expression levels and the estimated abundance of immune cell
207 infiltration while adjusting for tumor purity. Immune infiltration estimates were derived from
208 multiple deconvolution algorithms integrated within TIMER3.0, covering major immune cell
209 populations, including B cells, CD4⁺ and CD8⁺ T cells, natural killer (NK) cells, macrophages,
210 dendritic cells, neutrophils, and mast cells, as well as refined immune subsets and activation
211 states. Correlation coefficients and statistical significance were visualized using heatmap
212 representations, enabling a comprehensive assessment of the potential role of LPL in shaping
213 tumor-immune interactions across cancers.

214 **8. Functional enrichment analysis**

215 To investigate the biological significance of LPL expression in head and neck squamous cell

216 carcinoma (HNSC), transcriptomic data were downloaded from The Cancer Genome Atlas
217 (TCGA) via the UCSC Xena browser (<https://xenabrowser.net/>). Patient samples from the
218 TCGA-HNSC cohort were stratified into high- and low-LPL expression groups based on the
219 median expression level. Differential gene expression analysis was performed using the “limma”
220 package in R, with thresholds set at $|\log_2 \text{fold change}| > 1$ and adjusted p-value < 0.05 to identify
221 significantly altered genes associated with LPL expression.

222 To further interpret the biological roles of these differentially expressed genes, Gene Ontology
223 (GO) term annotation and Kyoto Encyclopedia of Genes and Genomes (KEGG) pathway
224 enrichment analyses were performed using the “clusterProfiler” R package. GO terms were
225 categorized into biological processes (BP), cellular components (CC), and molecular functions
226 (MF). Results were visualized as bar charts and bubble plots using the “ggplot2” and
227 “enrichplot” packages.

228 Additionally, gene set enrichment analysis (GSEA) was conducted to evaluate the global
229 pathway associations of LPL expression. Curated gene sets for GO and KEGG were retrieved
230 from the MSigDB database (v7.5.1). Samples were ranked by the signal-to-noise ratio between
231 expression groups, and normalized enrichment scores (NES) were calculated using 1000
232 permutations. Multiple testing correction was performed using the Benjamini–Hochberg false
233 discovery rate (FDR) method. Adjusted P values (FDR-q values) were used to determine
234 statistical significance, and pathways/terms with adjusted $P < 0.05$ were considered
235 significantly enriched. All analyses were implemented in R software (version 4.3.1).

236 **9. Molecular dynamics simulation of DBP–LPL interaction**

237 To assess the binding interaction between di-*n*-butyl phthalate (DBP) and lipoprotein lipase
238 (LPL), molecular docking followed by molecular dynamics (MD) simulations was conducted.
239 The predicted three-dimensional structure of human LPL was obtained from the AlphaFold
240 Protein Structure Database (<https://alphafold.ebi.ac.uk/>) under the accession AF-P06858-F1.
241 The molecular structure of DBP (PubChem CID: 3026) was downloaded in SDF format and
242 converted to PDBQT using AutoDock Tools 1.5.7. Structural preparation of the protein
243 involved removal of crystallographic water, addition of hydrogen atoms, and assignment of

244 partial atomic charges.

245 MD simulations of the LPL–DBP complex were performed using the GROMACS 2022.4
246 software suite. The Amber14SB force field was applied for protein parameters, and GAFF2
247 parameters for DBP were generated using the Antechamber module from AmberTools. Ligand
248 topologies were converted to GROMACS format with ACPYPE. The initial complex structure
249 derived from molecular docking was solvated in a dodecahedral TIP4P water box with
250 appropriate ion placement to simulate physiological ionic strength (0.15 M). Periodic boundary
251 conditions and Particle Mesh Ewald (PME) methods were employed for accurate electrostatics.

252 Following energy minimization and equilibration phases under NVT and NPT conditions, a 100
253 ns production run was carried out. Trajectory analyses included the calculation of root-mean-
254 square deviation (RMSD), root-mean-square fluctuation (RMSF), radius of gyration (Rg),
255 solvent-accessible surface area (SASA), and hydrogen bond formation. Binding free energy
256 (ΔG_{bind}) was estimated using the MM/GBSA method implemented via `gmx_MMPBSA`.

257 **10. Cell experiments**

258 **10.1. Cell culture**

259 The human hypopharyngeal squamous cell carcinoma cell line SCC9 was obtained from Procell
260 (Wuhan, China). Cells were maintained in Dulbecco's Modified Eagle Medium (DMEM; Gibco,
261 USA) supplemented with 10% fetal bovine serum (FBS; ExCell Bio, Uruguay) and 1%
262 penicillin–streptomycin (Biosharp, China). Cultures were incubated at 37 °C in a humidified
263 atmosphere containing 5% CO₂. Cells were subcultured using 0.25% trypsin–EDTA (Biosharp,
264 China).

265 **10.2. siRNA transfection**

266 For LPL knockdown, SCC9 cells were transfected with either LPL-specific siRNA or a
267 scrambled negative control siRNA (GenePharma, Shanghai, China). Transfections were
268 performed using Lipofectamine 3000 (Invitrogen, USA) in Opti-MEM serum-reduced medium
269 (Gibco, USA), according to the manufacturer's instructions. Cells were plated into 6-well plates
270 at an initial confluency of 40–50%, followed by transfection with 50 nM siRNA. After a 6-h

271 incubation period, the transfection medium was replaced with fresh, complete DMEM. Cells
272 were then cultured for an additional 24 to 48 h before proceeding to downstream assays. The
273 efficiency of LPL gene knockdown was verified using quantitative real-time PCR (qRT-PCR).

274 **10.3. Cell proliferation assay (CCK8)**

275 To assess the impact of DBP on the proliferative capacity of HNSC cells, SCC9 cells were
276 seeded into 96-well plates at a density of 4×10^3 cells per well and cultured overnight to allow
277 for attachment. Cells were subsequently exposed to varying concentrations of DBP (0, 0.1, 1,
278 and 10 μ M; MedChemExpress, USA) for different durations (0, 12, 24, 36, and 48 h).

279 At each indicated time point, 10 μ L of Cell Counting Kit-8 (CCK-8) reagent (Beyotime, China)
280 was added to each well, followed by incubation at 37 °C for 1 h. Absorbance was measured at
281 450 nm using a microplate reader (Thermo Fisher Scientific, USA) to determine cell viability.
282 All experiments were performed in triplicate, and data were presented as mean \pm standard
283 deviation (SD).

284 **10.4. Quantitative Real-Time PCR (qRT-PCR)**

285 Total RNA was isolated from SCC9 cells using TRIzol reagent (Sparkjade, China), following
286 the manufacturer's protocol. First-strand cDNA synthesis was carried out using the Evo M-
287 MLV RT Mix Kit (Sparkjade, China). Quantitative real-time PCR was conducted with SYBR
288 Green Premix Pro Taq HS qPCR Kit (Sparkjade, China) on a LightCycler 480 II detection
289 system (Roche, Switzerland).

290 Primers for LPL, PIK3CA, AKT1, mTOR and the internal reference gene β -actin were
291 synthesized by General Biosystems (Anhui, China). Relative mRNA expression levels were
292 calculated using the $2^{-\Delta\Delta C_t}$ method. Each reaction was performed in technical triplicates to
293 ensure reproducibility.

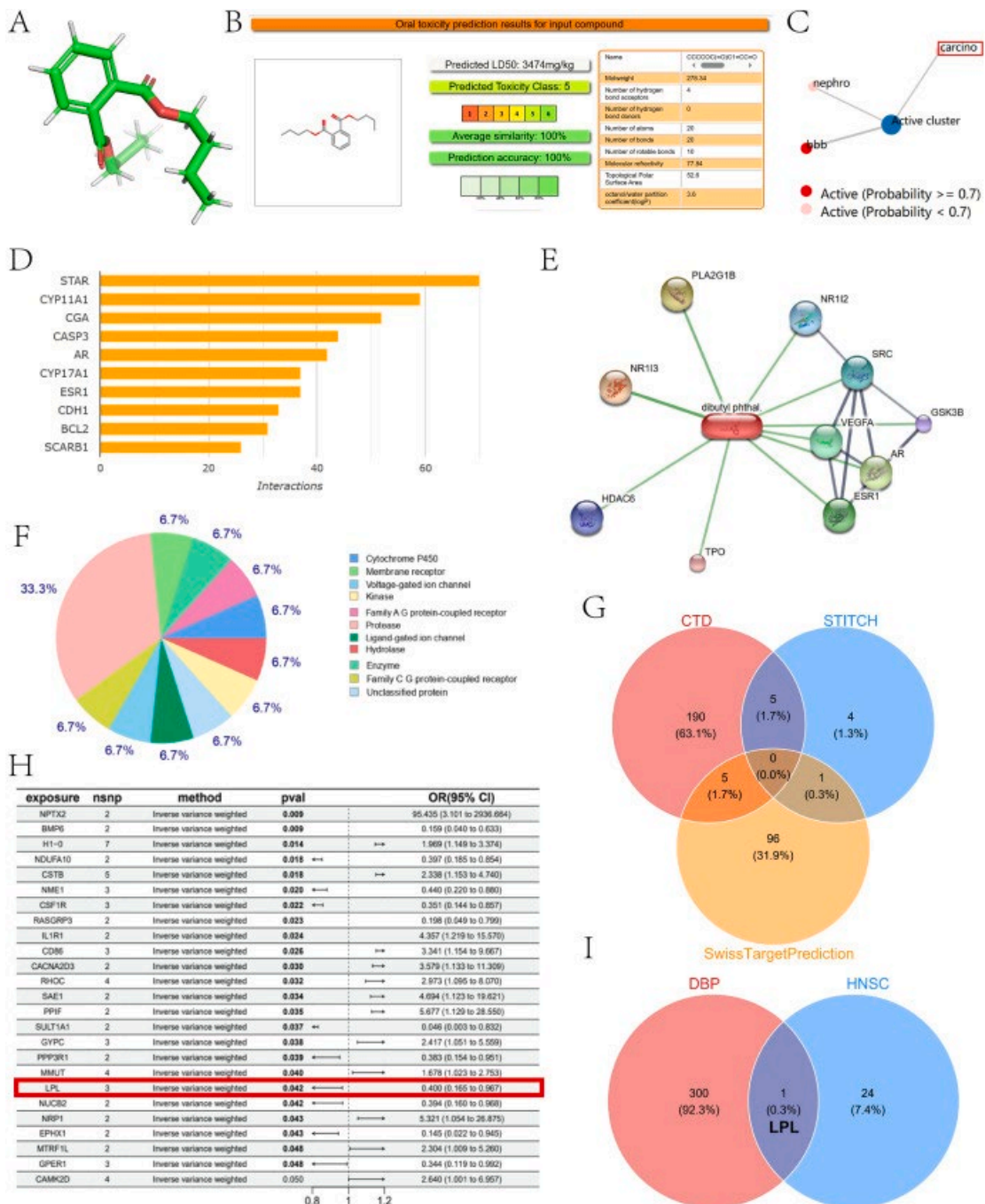
294

295

296 **11. Results**

297 **11.1. Network toxicology and Mendelian randomization analysis of DBP in HNSC**

298 The three-dimensional molecular structure of di-*n*-butyl phthalate (DBP) is illustrated in Fig.
 299 1A. Toxicity prediction using the Protox web server indicated that DBP belongs to toxicity class
 300 5, with a predicted oral LD₅₀ of 3474 mg/kg (Fig. 1B). DBP demonstrated a high prediction
 301 accuracy (100%) and structural similarity (100%) to known toxic compounds, suggesting
 302 moderate acute toxicity. Among the evaluated endpoints, DBP was predicted to be active in
 303 carcinogenicity with a high probability (Fig. 1C).



305 **Fig. 1. Network toxicology and Mendelian randomization analysis of DBP in HNSC.**

306 (A) Three-dimensional molecular structure of DBP. (B) Predicted oral toxicity and
307 physicochemical properties of DBP generated using the Protox platform, including LD₅₀,
308 toxicity class, and structural alerts. (C) Toxicity prediction network clustering DBP into an
309 active carcinogenicity cluster based on structural similarity. (D) Top 10 predicted DBP target
310 genes identified from the CTD database based on interaction strength. (E) PPI network of DBP
311 targets constructed using the STRING database. (F) Functional classification of DBP-
312 associated proteins based on molecular type and pathway involvement. (G) Venn diagram
313 showing the intersection of DBP targets across CTD, STITCH, and SwissTargetPrediction
314 databases. (H) Mendelian randomization analysis of DBP-related targets associated with HNSC.
315 The IVW estimate for LPL showed an OR of 0.400 (95% CI: 0.165–0.967, P = 0.042),
316 indicating that genetically predicted higher LPL levels are associated with reduced HNSC risk
317 and supporting LPL as a candidate protective factor. (I) Venn diagram showing LPL as the sole
318 intersecting gene between DBP-related targets and HNSC-associated genes.

319 **Abbreviations:** DBP, dibutyl phthalate; HNSC, head and neck squamous cell carcinoma; CTD,
320 Comparative Toxicogenomics Database; PPI, protein–protein interaction; MR, Mendelian
321 randomization; IVW, inverse variance weighted; OR, odds ratio; CI, confidence interval.

322

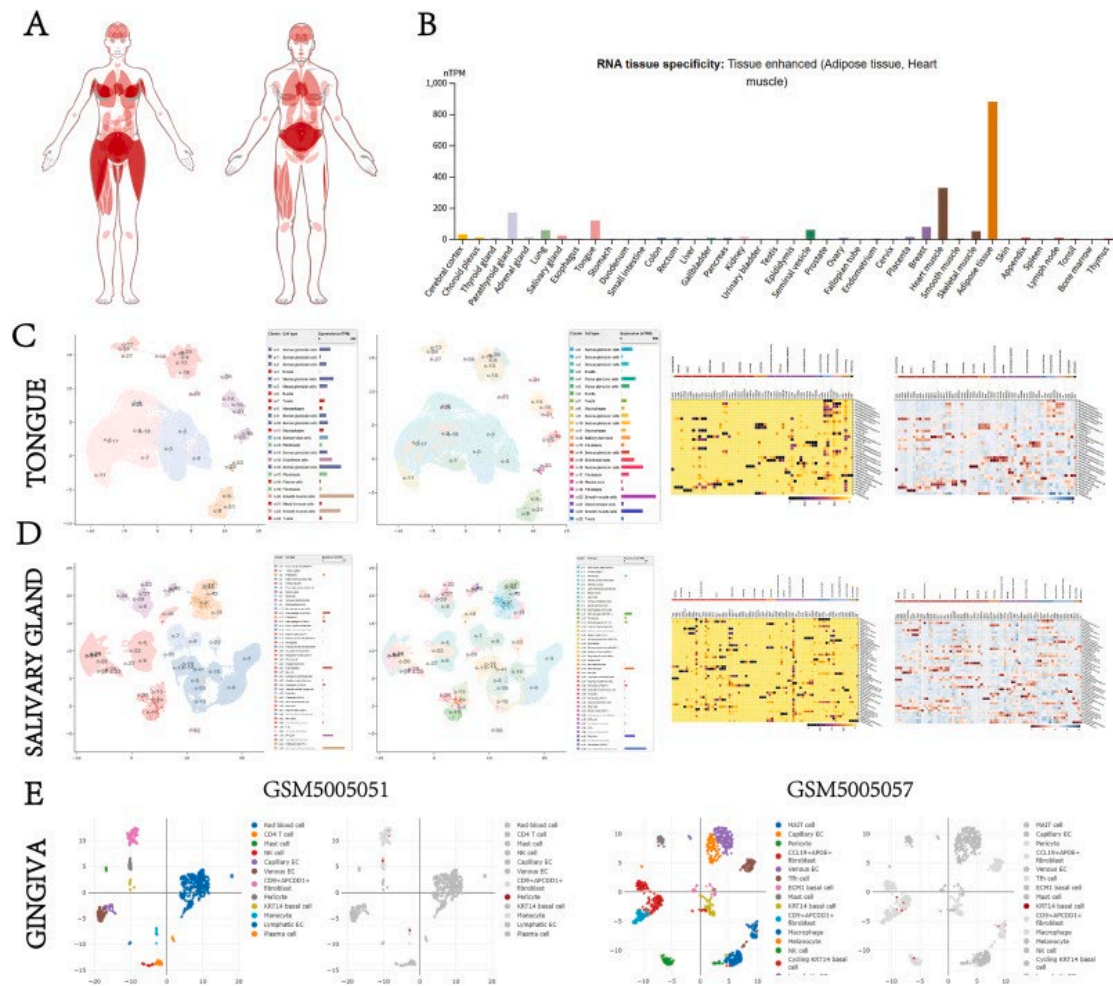
323 Candidate targets of DBP were identified from the SwissTargetPrediction, STITCH, and CTD
324 databases. Among these, the top 10 targets from the CTD database with the strongest interaction
325 evidence included STAR, CYP11A1, CGA, CASP3, AR, CYP17A1, ESR1, CDH1, BCL2, and
326 SCARB1 (Fig. 1D). To elucidate functional interactions, a protein–protein interaction (PPI)
327 network was constructed using the STRING database, revealing that DBP may interact with
328 key regulators involved in endocrine signaling and transcriptional control, such as AR, VEGFA,
329 ESR1, and GSK3B (Fig. 1E). Functional classification of DBP-related proteins retrieved from
330 SwissTargetPrediction indicated that the most abundant classes included kinases, enzymes,
331 membrane receptors, and nuclear receptors (Fig. 1F).

332 Integration of DBP target data from CTD, STITCH, and SwissTargetPrediction yielded a total

333 of 301 shared candidate genes (Fig. 1G). To assess potential causal relationships with head and
334 neck squamous cell carcinoma (HNSC), Mendelian randomization (MR) analysis was
335 conducted using genome-wide association summary statistics. MR analysis using the IVW
336 method indicated that genetically predicted higher LPL levels were significantly associated
337 with a lower risk of HNSC (OR = 0.400, 95% CI: 0.165–0.967, P = 0.042), supporting a
338 protective role of LPL in HNSC (Fig. 1H). Further intersection analysis between DBP-related
339 targets and HNSC-associated genes revealed LPL as the sole overlapping gene among 301
340 candidate targets (Fig. 1I). Collectively, these findings indicate that LPL may mediate part of
341 DBP's toxicological effects in HNSC and serve as a functional node connecting environmental
342 exposure to cancer susceptibility.

343 **11.2. Multi-level expression profiling and evolutionary conservation of LPL**

344 Based on transcriptomic and proteomic data from the Human Protein Atlas (HPA), DISCO, and
345 UCSC databases, we systematically characterized the multi-level expression and evolutionary
346 features of LPL across human tissues and cell types (Fig. 2, Fig. 3).



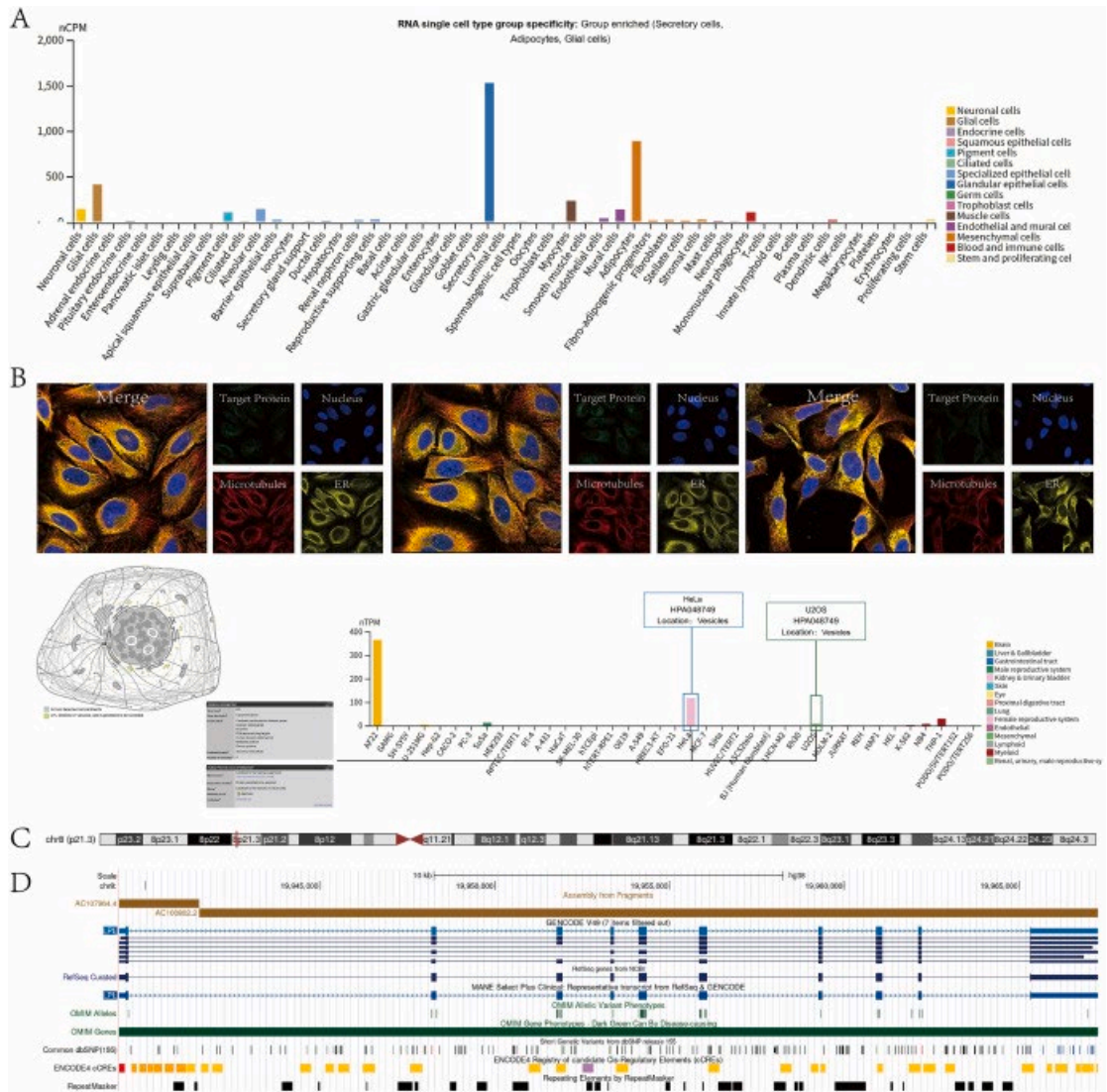
347

348 **Fig. 2. Expression landscape and cellular distribution of LPL in normal human tissues**
 349 **and head and neck-related organs.**

350 (A) Tissue RNA expression profile of LPL across normal human organs based on the HPA
 351 database, with color intensity indicating transcript abundance. (B) Quantitative RNA expression
 352 levels of LPL (nTPM) across normal human tissues, showing marked enrichment in adipose
 353 tissue, heart, and skeletal muscle. (C) Single-cell RNA-sequencing analysis of tongue tissue.
 354 UMAP projections illustrate cell type clustering, with LPL expression predominantly localized
 355 to schwann cells and smooth muscle/pericyte-related populations. (D) Single-cell RNA-
 356 sequencing analysis of salivary gland tissue, showing preferential expression of LPL in non-
 357 myelinated schwann cell, pericytes, and macrophages. (E) Single-cell RNA-sequencing
 358 analysis of gingival tissue (GSM5005051 and GSM5005057). UMAP clustering and expression
 359 mapping reveal significant enrichment of LPL in KRT14 basal cell and pericytes, with
 360 negligible expression in immune cell populations.

361 **Abbreviations:** HPA, Human Protein Atlas; UMAP, uniform manifold approximation and
 362 projection; nTPM, normalized transcripts per million. (For interpretation of the references to
 363 color in this figure legend, the reader is referred to the Web version of this article.)

364



365

366 Fig. 3. Single-cell expression, subcellular localization, and genomic conservation of LPL.

367 (A) Single-cell group-level RNA expression analysis of LPL based on the HPA database. LPL
 368 is annotated as a group-enriched gene, with preferential expression in secretory cells,
 369 adipocytes, and glial cells. Expression levels are shown as normalized counts per million
 370 (nCPM). (B) Subcellular localization of LPL protein assessed by immunofluorescence staining.
 371 LPL predominantly localizes to cytoplasmic vesicle-like structures and shows partial

372 colocalization with the endoplasmic reticulum (ER) and microtubules. Representative images
373 from different cell lines are shown. (C) Chromosomal localization of the LPL gene, indicating
374 its position on human chromosome 8p21.3. (D) Genomic architecture and regulatory features
375 of the LPL locus visualized using the UCSC Genome Browser, including exon–intron
376 organization, RefSeq and GENCODE transcript annotations, known genetic variants, and
377 candidate cCREs.

378 **Abbreviations:** nCPM, normalized counts per million; cCREs, candidate *cis*-regulatory
379 elements.

380

381 At the tissue level (Fig. 2A and B), RNA expression profiling in HPA showed that LPL displays
382 a highly tissue-specific expression pattern in normal human tissues. At the tissue level, LPL
383 transcripts were predominantly enriched in adipose tissue, heart, and skeletal muscle, while
384 relatively low expression was observed in most visceral organs and immune-related tissues.
385 According to HPA tissue specificity annotation, LPL is classified as a tissue-enhanced gene,
386 with the highest expression levels detected in adipose tissue, followed by cardiac and skeletal
387 muscle, consistent with its established metabolic functions.

388 At the single-cell level (Fig. 2C), analysis of tongue scRNA-seq data revealed a pronounced
389 cell type–specific distribution of LPL expression. UMAP clustering showed that LPL
390 expression was primarily localized to schwann cells and smooth muscle/pericyte-related
391 populations., whereas epithelial cells and the majority of immune cell subsets exhibited
392 minimal expression.

393 A similar expression pattern was observed in salivary gland tissue (Fig. 2D), where LPL was
394 preferentially expressed in non-myelinated schwann cell, pericytes, and macrophages, but
395 showed limited expression in acinar cells, ductal epithelial cells, and immune cells. These
396 findings indicate that LPL shows a stable and cell type–specific distribution across tongue and
397 salivary gland tissues, with predominant expression in neural-associated cells and vascular-
398 supporting populations, highlighting a potential role in metabolic maintenance of the local
399 neurovascular microenvironment.

400 Further analysis of two independent gingival scRNA-seq datasets from the DISCO database
401 (GSM5005051 and GSM5005057) (Fig. 2E) demonstrated highly consistent results. In both
402 datasets, LPL expression was strongly enriched in KRT14 basal cell and pericytes, with
403 negligible expression detected in T cells, B cells, NK cells, macrophages, and other immune
404 populations. Collectively, the cell type-specific enrichment of LPL in KRT14⁺ basal cells and
405 pericytes points toward a role in epithelial-vascular metabolic support and tissue homeostasis,
406 rather than immune-driven inflammatory processes.

407 To further comprehensively characterize the cell type specificity, subcellular localization, and
408 genomic features of LPL, we performed an integrated analysis using data from the Human
409 Protein Atlas (HPA), including single-cell group-level expression profiles,
410 immunofluorescence-based protein localization, and genome annotation.

411 At the single-cell group level (Fig. 3A), LPL exhibited a pronounced cell group-specific
412 expression pattern. Quantitative RNA analysis annotated LPL as a group-enriched gene, with
413 preferential expression in secretory cells, adipocytes, and glial cell populations. Among these
414 groups, adipocytes and secretory cells showed markedly higher LPL expression compared with
415 other cell types, whereas most immune cell populations and proliferative cell groups displayed
416 minimal expression. These results further support a functional association of LPL with
417 metabolic support and tissue homeostasis rather than immune or proliferative processes.

418 At the subcellular level (Fig. 3B), immunofluorescence-based protein localization analysis
419 demonstrated that LPL protein predominantly localized to cytoplasmic vesicle-like structures,
420 showing partial colocalization with the endoplasmic reticulum (ER) and microtubule networks.
421 Consistent vesicular localization patterns were observed across different cell lines, including
422 HeLa and U2OS cells, suggesting that LPL may be involved in vesicle-associated transport or
423 secretion pathways related to intracellular lipid handling and metabolic regulation.

424 At the genomic level (Fig. 3C and D), chromosomal mapping revealed that LPL is located on
425 chromosome 8p21.3. Further genome browser analysis showed that the LPL locus possesses a
426 relatively complex gene structure with multiple exons and transcript isoforms, accompanied by
427 a dense distribution of regulatory elements, including candidate *cis*-regulatory elements

428 (cCREs), as well as numerous annotated genetic variants. These features indicate that LPL
429 expression is subject to multilayered transcriptional regulation and potential genetic modulation.

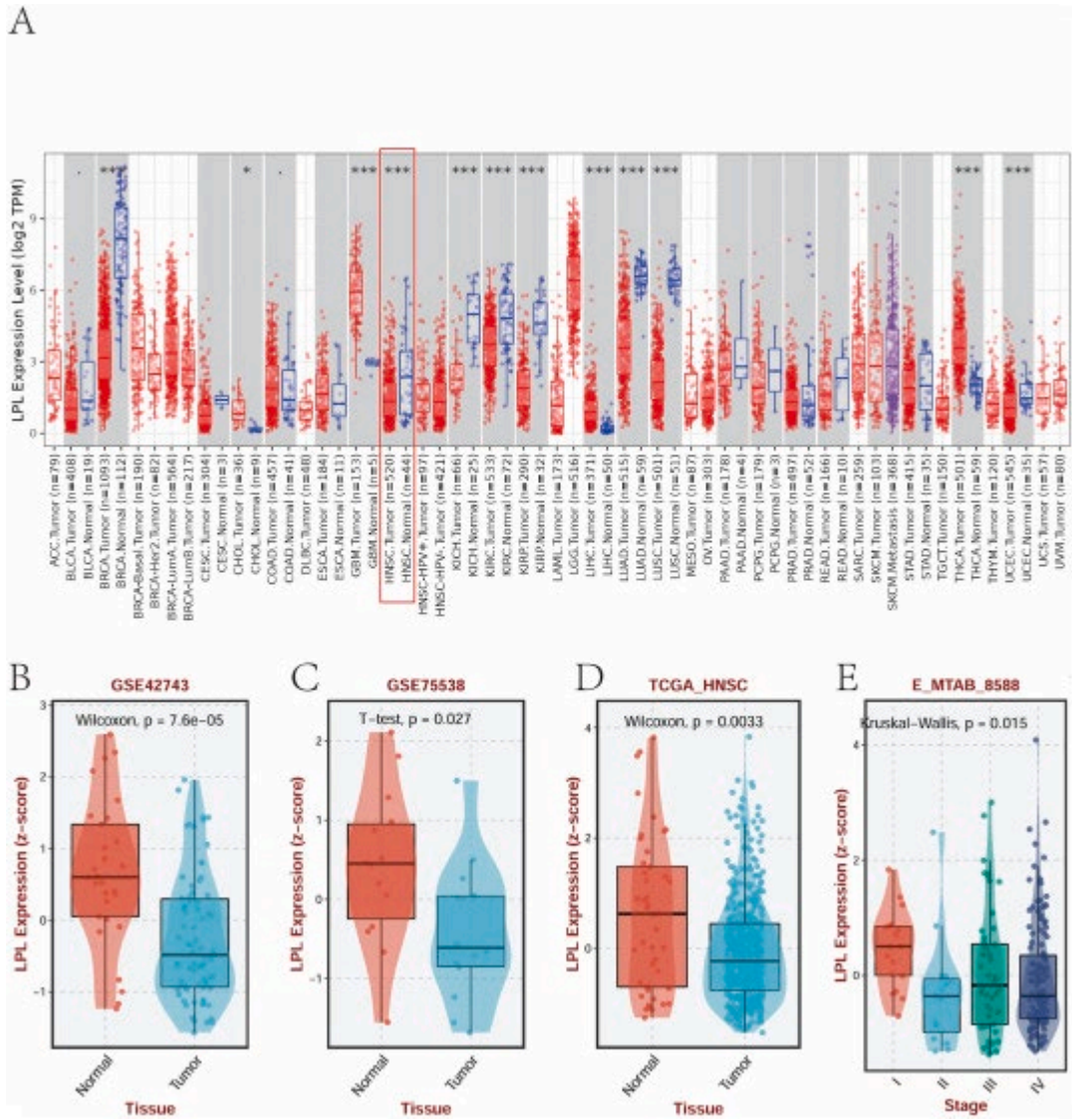
430

431 **11.3. Expression of LPL in HNSC and its clinical relevance**

432 We first used the TIMER2.0 database to evaluate differential LPL expression between tumor
433 and normal tissues across multiple cancer types. LPL exhibited heterogeneous expression
434 patterns among different malignancies, and in HNSC, LPL expression was significantly higher
435 in tumor tissues than in normal tissues (Fig. 4A). To assess the robustness of this observation,
436 we further analyzed independent HNSC cohorts available in the BEST database (Fig. 4B–D).
437 In the TCGA-HNSC, GSE42743, and GSE75538 cohorts, LPL expression was consistently and
438 significantly elevated in tumor tissues compared with normal tissues. Notably, LPL expression
439 was significantly associated with tumor stage in HNSC and showed an overall tendency to
440 decrease with increasing stage (Fig. 4E), suggesting that LPL expression may be related to
441 disease progression in HNSC.

442 **11.4. Genomic alterations and immune Modulatory associations of LPL**

443 To comprehensively evaluate the genomic alterations of LPL and their potential immunological
444 relevance, we integrated multi-platform data from the cBioPortal and TIMER3.0 databases to
445 systematically analyze somatic mutations, copy number alterations (CNAs), and structural
446 variants in head and neck squamous cell carcinoma (HNSC) (Fig. 5).



447

448 **Fig. 5. Landscape of LPL genomic alterations across TCGA cancers.**

449 (A) OncoPrint visualization of LPL genomic alterations across TCGA HNSC datasets, showing
 450 mutations, copy number alterations (amplification, gain, shallow deletion, and deep deletion),
 451 and structural variants, together with study origin and profiling status. (B) Frequency of LPL
 452 genomic alterations across head and neck squamous cell carcinoma and related tumor cohorts,
 453 categorized by alteration type, including deep deletion, mutation, and amplification. (C)
 454 Distribution of LPL mutation counts across HNSC-related cancer subtypes, illustrating the low
 455 mutation burden of LPL within head and neck squamous malignancies. (D) Proportion of
 456 samples with different LPL copy number alteration states across TCGA tumor types, including
 457 deep deletion, arm-level deletion, diploid/normal, arm-level gain, and high-level amplification.
 458 (E) Frequency of LPL somatic mutations across TCGA cancers, highlighting the relatively low

459 mutation rate of LPL in HNSC compared with other tumor entities.

460 **Abbreviations:** TCGA, The Cancer Genome Atlas.

461

462 As summarized in the OncoPrint analysis (Fig. 5A), LPL alterations were detected in
463 approximately 1% of HNSC and related tumor samples. These alterations were predominantly
464 characterized by deep deletions, with occasional missense mutations of unknown significance
465 and rare amplification events, while somatic mutations were generally infrequent.

466 Further comparative analysis demonstrated that the frequency of LPL alterations varied across
467 different tumor types (Fig. 5B). Among the analyzed cancers, LPL alterations were mainly
468 driven by deep deletions, which represented the predominant alteration type in most tumor
469 entities. In contrast, structural variant-associated alterations were rare across all cancer types,
470 and the overall alteration frequency of LPL remained below 3%.

471 Consistent with these observations, mutation count analysis revealed that LPL mutations
472 occurred at low frequencies across multiple cancer subtypes, including HNSC (Fig. 5C). Most
473 tumor samples harbored no detectable LPL mutations or only a very limited number of events,
474 indicating that LPL is not a highly mutated gene in solid malignancies.

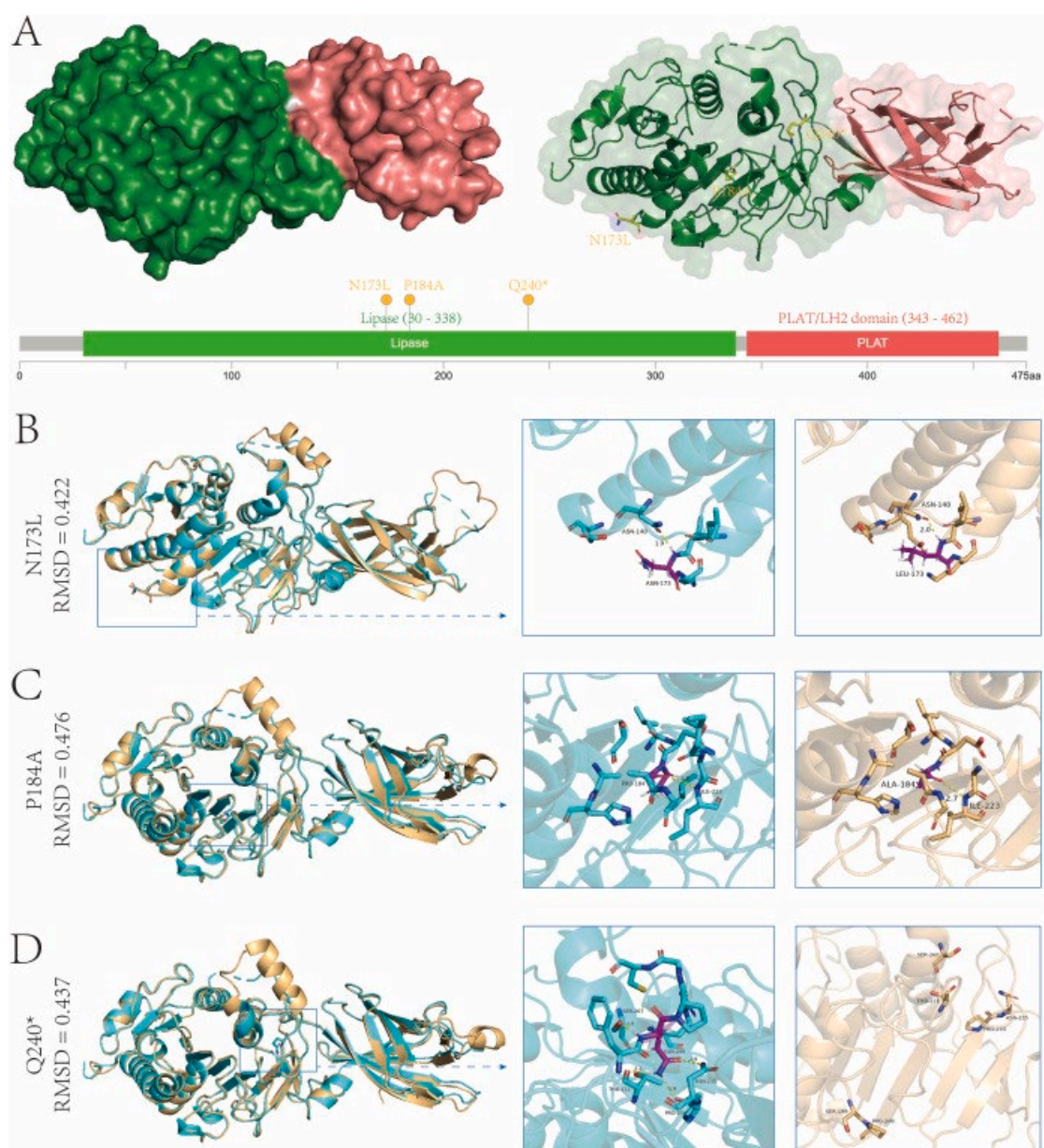
475 Analysis of LPL copy number status in TCGA cohorts further revealed substantial inter-tumor
476 heterogeneity in CNA patterns (Fig. 5D). In HNSC, arm-level deletions were the predominant
477 CNA event, accompanied by a smaller proportion of diploid/normal status and arm-level gains,
478 suggesting that LPL alterations in head and neck squamous cell carcinoma are mainly driven
479 by copy number loss.

480 Finally, mutation frequency analysis confirmed that somatic mutations of LPL were uncommon
481 across various cancer types (Fig. 5E). In HNSC, LPL mutations were detected in only 3 out of
482 509 samples, occurring at a lower frequency compared with several other tumor types. These
483 findings further support the conclusion that genomic alterations of LPL in HNSC are primarily
484 characterized by copy number variation rather than sequence-level mutations.

485

486 **11.5. Structural and Mutation Site Analysis of LPL**

487 As shown in Fig. 6A, the full-length LPL protein consists of an N-terminal lipase domain
488 (residues 30–338) and a C-terminal PLAT/LH2 domain (residues 343–462). All three mutations
489 identified in the TCGA-HNSC cohort—N173L, P184A, and Q240*—are located within the
490 lipase domain, spatially distant from the PLAT domain, suggesting that their primary effects
491 are likely mediated through alterations in the catalytic or structural core of LPL.



492

493 **Fig. 6. Structural and Mutation Site Analysis of LPL**

494 (A) Three-dimensional structure of LPL showing protein domains and the locations of the three

495 mutation sites. (B–D) Structural alignment of mutant and wild-type LPL proteins, highlighting
496 residues within 4 Å of the mutation sites and associated hydrogen bonds.

497

498 Structural superimposition of the N173L mutant with the wild-type LPL protein (Fig. 6B)
499 revealed a high degree of overall structural similarity, with a C α RMSD of 0.422 Å, indicating
500 minimal global conformational deviation. At the local level, detailed inspection of residues
501 within 4 Å of the mutation site showed that the hydrogen bond between residue 173 and ASN-
502 140 was preserved after substitution. The local backbone conformation and side-chain
503 orientation remained largely unchanged, and no apparent displacement of surrounding
504 secondary structural elements was observed. Together, these features suggest that the N173L
505 substitution induces only subtle local perturbations and is unlikely to markedly disrupt the
506 overall structural integrity of the lipase domain. In contrast, the P184A mutant exhibited the
507 largest RMSD (0.476 Å) among the three variants (Fig. 6C), indicating a modest increase in
508 global structural deviation relative to the wild-type protein. Locally, replacement of the
509 conformationally restrictive proline with alanine resulted in increased side-chain flexibility in
510 the surrounding region. Nevertheless, the hydrogen bond interaction between ALA-184 and
511 ILE-223 was retained, and the neighboring residues within the 4 Å radius remained relatively
512 compact. These observations suggest that although the P184A mutation introduces local
513 conformational relaxation, it does not abolish key stabilizing interactions and therefore may
514 exert a moderate but structurally tolerable effect on the lipase domain. The Q240* truncation
515 mutation displayed distinct structural characteristics compared with the two missense variants
516 (Fig. 6D). Structural alignment of the truncated protein with the wild-type LPL revealed a C α
517 RMSD of 0.437 Å within the aligned region, indicating detectable conformational deviation.
518 Notably, local analysis of residues originally located within 4 Å of the truncation site
519 demonstrated a pronounced loss of structural compactness, accompanied by the disappearance
520 of four hydrogen bonds present in the wild-type structure. The remaining residues surrounding
521 the truncation site appeared more spatially dispersed, suggesting a reduction in local stabilizing
522 interactions.

523 Given that Q240* results in the deletion of downstream amino acid sequences within the lipase

541 assessed by TIMER3.0. Analyses were adjusted for tumor purity. Immune cell populations
542 include major immune lineages (B cells, CD4⁺ and CD8⁺ T cells, NK cells, macrophages, and
543 dendritic cells) as well as refined immune subsets and activation states. Color intensity
544 represents the direction and magnitude of the correlation, and symbols indicate statistical
545 significance.

546 **Abbreviations:** TIMER, Tumor Immune Estimation Resource. (For interpretation of the
547 references to color in this figure legend, the reader is referred to the Web version of this article.)

548

549 Specifically, LPL expression showed significant positive correlations with multiple immune
550 cell populations, including B cells, CD4⁺ T cells, regulatory T cells (Tregs), dendritic cells, and
551 macrophages. These associations spanned both adaptive and innate immune compartments,
552 indicating that LPL expression is linked to the overall enrichment of diverse immune cell
553 lineages rather than to a single immune subset.

554 In addition to immune cells, LPL expression was also positively correlated with several non-
555 immune stromal components, including endothelial cells, hematopoietic stem cells, and cancer-
556 associated fibroblasts (CAFs). These findings suggest that LPL expression is associated with
557 vascular, mesenchymal, and supportive elements of the tumor microenvironment, highlighting
558 its potential relevance to the structural organization of tumor tissues.

559 Taken together, LPL expression did not display a cell type–restricted correlation pattern, but
560 instead showed coordinated positive associations with both immune and stromal compartments.
561 This integrated correlation profile indicates that LPL expression levels may reflect the overall
562 immune–stromal enrichment and increased microenvironmental complexity within tumors,
563 rather than serving as a marker of isolated immune cell populations.

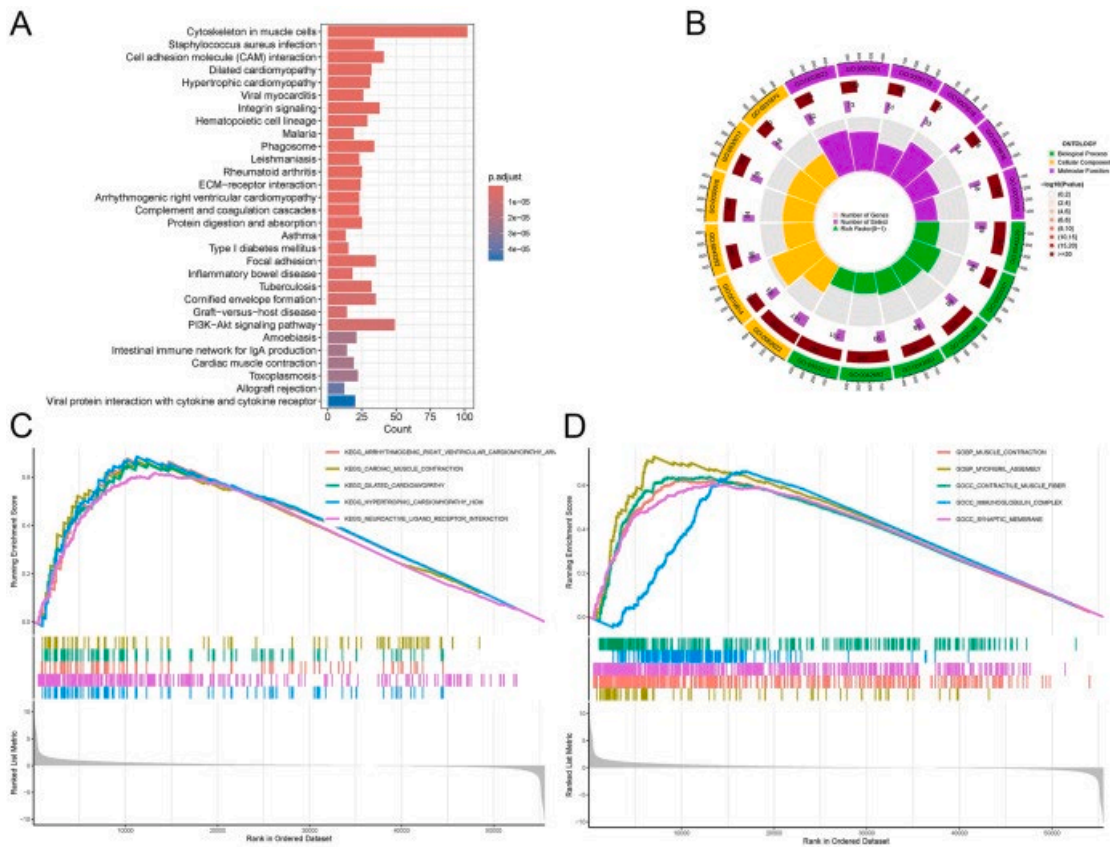
564

565 **11.7. Functional enrichment analysis of LPL in HNSC**

566 To investigate the biological relevance of LPL in head and neck squamous cell carcinoma
567 (HNSC), enrichment analyses were performed based on transcriptomic profiles from the

568 TCGA-HNSC dataset.

569 KEGG pathway analysis revealed that LPL-associated genes were significantly enriched in
570 pathways related to immune response, cytoskeletal dynamics, and signal transduction,
571 including “*Staphylococcus aureus* infection,” “ECM–receptor interaction,” “PI3K–Akt
572 signaling,” and “cardiac muscle contraction” (Fig. 8A). These findings suggest that LPL may
573 participate in immune modulation and structural remodeling in the tumor microenvironment.



574

575 **Fig. 8. Functional enrichment analysis of LPL-associated genes in head and neck**
576 **squamous cell carcinoma (HNSC).**

577 (A) KEGG pathway enrichment analysis revealing significant involvement of LPL-related
578 genes in muscle contraction, immune regulation, PI3K–Akt signaling, cell adhesion, and
579 inflammatory processes. (B) Gene Ontology (GO) annotation results showing enriched terms
580 across three major categories: biological process (BP), cellular component (CC), and molecular
581 function (MF). The inner circle denotes the number of genes involved, while the outer ring
582 indicates the gene ratio and statistical significance. (C) Gene set enrichment analysis (GSEA)

583 based on KEGG pathways demonstrating enrichment in cardiomyopathy, calcium signaling,
584 and ligand–receptor interaction pathways in the high LPL expression group. (D) GSEA based
585 on GO terms showing strong enrichment in actomyosin assembly, contractile fiber organization,
586 and membrane-associated components related to elevated LPL expression.

587 **Abbreviations:** KEGG, Kyoto Encyclopedia of Genes and Genomes; GO, Gene Ontology; BP,
588 biological process; CC, cellular component; MF, molecular function; GSEA, gene set
589 enrichment analysis.

590

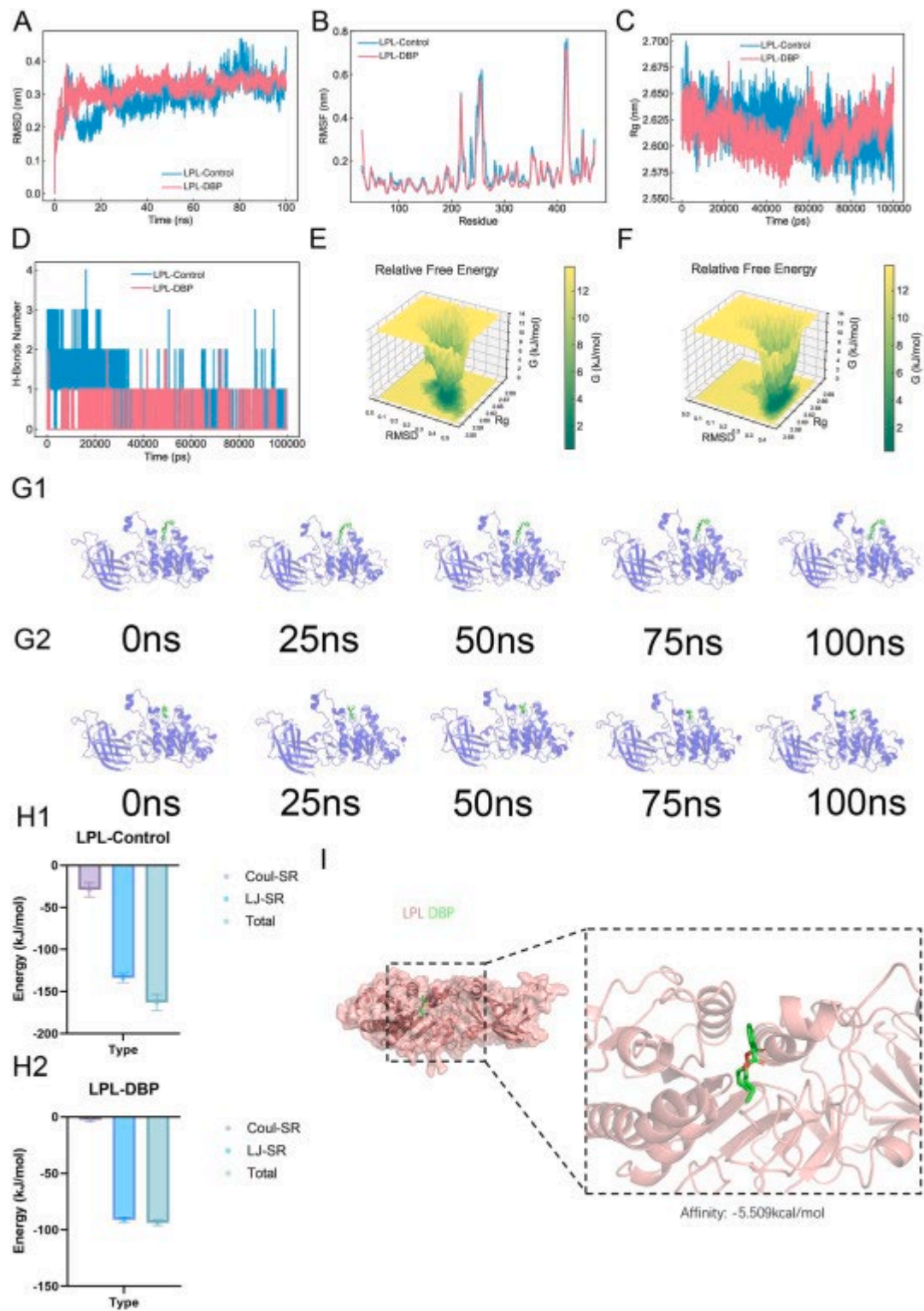
591 GO annotation analysis showed that enriched biological processes were primarily linked to
592 muscle contraction and actin filament organization. In terms of cellular components and
593 molecular functions, enriched terms included “contractile fiber,” “sarcomere,” and “actin
594 binding” (Fig. 8B), indicating LPL involvement in cytoskeletal organization.

595 GSEA further confirmed that genes upregulated in the LPL-high expression group were
596 enriched in KEGG pathways such as “dilated cardiomyopathy” and “cytokine receptor
597 interaction” (Fig. 8C). GO-based GSEA also highlighted enrichment in terms like “muscle
598 contraction” and “myofibril assembly” (Fig. 8D).

599 Overall, these results suggest that LPL may influence HNSC progression by regulating
600 pathways associated with immune response and structural integrity.

601 **11.8. Molecular dynamics simulation of the LPL–DBP complex**

602 To investigate the structural dynamics and binding stability of DBP with LPL, a 100 ns
603 molecular dynamics simulation was performed and compared to apo LPL. The root-mean-
604 square deviation (RMSD) trajectory showed that both systems reached equilibrium after
605 approximately 20 ns (Fig. 9A). However, the LPL–DBP complex exhibited slightly higher
606 structural fluctuations over the simulation period, suggesting moderate conformational
607 adaptation upon ligand binding.



608

609 **Fig. 9. Molecular dynamics simulations of LPL–DBP interaction.**

610 (A) RMSD trajectories of apo LPL and LPL–DBP complex, indicating minor structural
 611 deviation upon ligand binding. (B) Per-residue RMSF analysis showing local flexibility
 612 differences, with subtle stabilization near the DBP binding region. (C) Radius of gyration (Rg)

613 plots comparing global compactness of free LPL versus the DBP-bound complex. (D)
614 Hydrogen bond numbers formed between LPL and DBP, reflecting interaction stability
615 throughout the simulation. (E–F) Free-energy landscapes (FEL) projected onto RMSD and Rg
616 dimensions for apo LPL (E) and the LPL–DBP complex (F), showing distinct conformational
617 energy basins. (G1–G2) Representative structural snapshots of apo LPL (G1) and LPL–DBP
618 complex (G2) extracted at 0,25,50,75,100ns, demonstrating stable ligand accommodation.
619 (H1–H2) MM/GBSA decomposition of binding free energy for apo LPL (H1) and the LPL–
620 DBP complex (H2), illustrating contributions from electrostatic (Coul-SR), van der Waals (LJ-
621 SR), and total interaction energies. (I) Final binding conformation of DBP (green) within the
622 LPL catalytic site, with predicted binding affinity of -5.509 kcal mol⁻¹.

623 **Abbreviations:** RMSD, root mean square deviation; RMSF, root mean square fluctuation; Rg,
624 radius of gyration; FEL, free-energy landscape; MM/GBSA, molecular mechanics/generalized
625 Born surface area. (For interpretation of the references to color in this figure legend, the reader
626 is referred to the Web version of this article.)

627

628 Residue-level root-mean-square fluctuation (RMSF) analysis revealed no substantial
629 differences in backbone flexibility between the control and DBP-bound systems, although
630 minor stabilization was observed around the binding site (Fig. 9B). The radius of gyration (Rg)
631 remained relatively stable in both systems, with only slight variations indicating similar global
632 compactness (Fig. 9C).

633 The number of hydrogen bonds formed between LPL and DBP fluctuated dynamically but
634 remained consistently present throughout the simulation, supporting the persistence of the
635 ligand–protein interaction (Fig. 9D). Free energy landscape (FEL) analysis based on RMSD
636 and Rg values demonstrated that the DBP-bound system sampled a narrower and deeper energy
637 basin compared to apo LPL, indicating enhanced conformational stability in the bound state
638 (Fig. 9E and F).

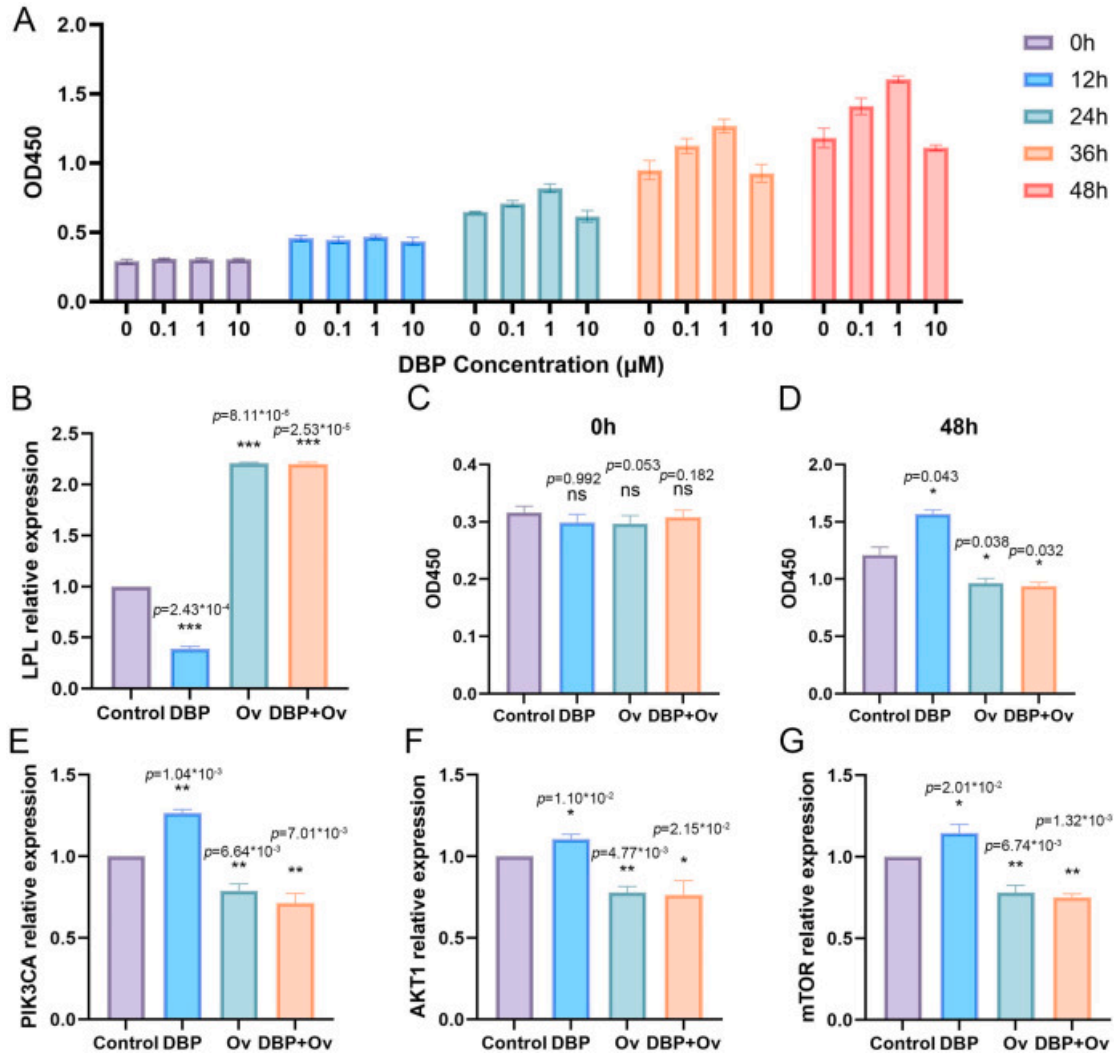
639 Structural snapshots taken at 25 ns intervals showed that DBP remained stably positioned in
640 the LPL binding pocket throughout the 100 ns simulation (Fig. 9G1–G2). MM/GBSA

641 calculations further revealed favorable binding energetics, with the total binding free energy of
642 the LPL–DBP complex estimated at -124.97 kJ/mol (Fig. 9H2), primarily driven by van der
643 Waals and electrostatic interactions. The docking conformation (Fig. 9I) confirmed that DBP
644 was embedded within the LPL catalytic cavity, with a predicted binding affinity of
645 -5.509 kcal/mol.

646 These results collectively suggest that DBP forms a stable and energetically favorable complex
647 with LPL, which may underlie its capacity to modulate LPL function at the molecular level.

648 **11.9. DBP promotes HNSC cell proliferation and is associated with PI3K–AKT–mTOR–** 649 **related transcriptional changes via LPL suppression**

650 To evaluate the effect of DBP on HNSC cell proliferation, SCC9 cells were treated with
651 increasing concentrations of DBP (0, 0.1, 1, and 10 μ M) for 0–48 h. CCK-8 results showed a
652 time- and dose-dependent increase in cell viability, with the most pronounced effect observed
653 at 1 μ M for 48 h (Fig. 10A).



654

655 **Fig. 10. DBP suppresses LPL expression and promotes cell proliferation via PI3K–AKT–**
 656 **mTOR signaling in HNSC cells.**

657 (A) CCK-8 assay showing time- and dose-dependent effects of DBP (0–10 μM) on SCC9 cell
 658 viability at 0, 12, 24, 36, and 48 h (B) qRT-PCR analysis of LPL mRNA expression under
 659 different conditions: control, DBP treatment, LPL overexpression (Ov), and combined
 660 DBP + Ov. (C–D) CCK-8 assay at 0 h (C) and 48 h (D) showing that DBP significantly
 661 promoted SCC9 cell proliferation after 48 h (E–G) Relative mRNA expression of PI3K
 662 pathway–related genes: PIK3CA (E), AKT1 (F), and mTOR (G). DBP upregulated all three,
 663 and this effect was reversed by LPL overexpression.

664 **Abbreviations:** CCK-8, Cell Counting Kit-8; qRT-PCR, quantitative real-time polymerase
 665 chain reaction; Ov, overexpression.

666 **Statistical notation:** Data are presented as mean \pm SD. ns, not significant; *P < 0.05,
667 **P < 0.01, ***P < 0.001 versus the Control group.

668

669 qRT-PCR analysis demonstrated that DBP significantly downregulated LPL mRNA levels,
670 whereas LPL overexpression restored its expression, even under DBP treatment (Fig. 10B).
671 CCK-8 assays further confirmed that DBP promoted SCC9 proliferation after 48 h, and this
672 effect was reversed by LPL overexpression (Fig. 10C and D), suggesting that LPL negatively
673 regulates DBP-induced proliferation.

674 To explore the underlying mechanism, we assessed the expression of key genes in the PI3K–
675 AKT–mTOR signaling pathway. DBP treatment led to upregulation of PIK3CA, AKT1, and
676 mTOR mRNA levels (Fig. 10E–G). Notably, LPL overexpression attenuated these
677 transcriptional changes, suggesting that LPL may be involved in the regulation of PI3K–AKT–
678 mTOR–related gene expression in HNSC cells.

679 Together, these results suggest that DBP enhances HNSC cell proliferation by downregulating
680 LPL and is associated with transcriptional changes in PI3K–AKT–mTOR–related genes.

681

682 **12. Discussion**

683 This study employed a network toxicology approach to integrate the action targets of the
684 environmental pollutant DBP with the key gene network of head and neck squamous cell
685 carcinoma (HNSC). The analysis revealed that LPL may serve as an intersecting gene and
686 functional link between them. Through combined evidence from bioinformatics and
687 experiments, we preliminarily clarified the potential protective role of LPL in DBP-associated
688 HNSC carcinogenesis. Analysis of the TCGA database indicated that LPL expression levels
689 were decreased in HNSC tumor tissues compared to normal tissues. In cellular experiments, we
690 observed that DBP exposure could alter LPL mRNA levels in HNSC cells (suggesting that this
691 environmental toxicant can regulate the expression of this metabolic gene) and affect tumor cell
692 viability. Results from molecular docking and molecular dynamics simulations further

693 demonstrated that DBP can stably bind to the LPL protein, suggesting that DBP may interact
694 with LPL at the structural level, although whether this interaction translates into functional
695 modulation of enzymatic activity requires further biochemical validation. Notably, molecular
696 docking and dynamics simulations primarily reflect binding stability and do not directly
697 demonstrate enzymatic inhibition. Therefore, additional biochemical assays, such as
698 triglyceride hydrolysis measurements, would be required to determine whether DBP binding
699 functionally suppresses LPL activity. Collectively, these findings support the hypothesis that
700 LPL exerts an anti-tumor effect in HNSC and untangle that DBP exposure may promote the
701 initiation and progression of HNSC by inhibiting or functionally antagonizing LPL.

702 Lipoprotein lipase (LPL), as a central regulator of lipid metabolism, exhibits a context-
703 dependent and functionally divergent role in tumor biology. This apparent duality is
704 increasingly recognized as a consequence of the dynamic interplay between tumor metabolic
705 demands and the tumor microenvironment (TME) (Wang et al., 2025). On one hand, in
706 metabolically active and lipid-rich tumor contexts, LPL facilitates the hydrolysis of circulating
707 triglyceride-rich lipoproteins, thereby releasing free fatty acids that can be readily utilized by
708 tumor cells (Fu et al., 2024; Ma et al., 2025). These exogenous lipids serve as critical substrates
709 for β -oxidation, membrane biosynthesis, and lipid signaling, ultimately supporting tumor
710 proliferation and survival. In such settings, elevated LPL activity may enhance metabolic
711 flexibility and contribute to tumor progression, particularly in cancers characterized by high
712 lipid dependency. For instance, studies in cancers such as lung cancer have shown that increased
713 LPL activity in tumor tissues is often associated with poorer patient survival, suggesting that
714 tumor cells acquiring nutrients via LPL to promote growth may accelerate disease progression
715 (Trost et al., 2009; Cerne et al., 2007). On the other hand, LPL may also exert tumor-suppressive
716 functions by remodeling the tumor microenvironment. Lipid metabolism is a key determinant
717 of immune cell function, and LPL-mediated lipid processing has been implicated in regulating
718 immune cell phenotypes, especially macrophage polarization. Increased LPL expression has
719 been associated with a shift toward a pro-inflammatory, anti-tumor M1-like macrophage
720 phenotype, whereas reduced LPL activity may contribute to an immunosuppressive, tumor-
721 promoting microenvironment (Yang et al., 2025). In the context of head and neck squamous

722 cell carcinoma (HNSC), we hypothesize that high LPL expression might help improve the
723 tumor immune microenvironment, such as by enhancing the function of anti-tumor immune
724 cells or suppressing pro-tumor inflammatory signals, thereby counteracting the carcinogenic
725 effects induced by DBP. The protective role of LPL observed in this study suggests that the
726 progression of HNSC under DBP exposure may be partly attributed to its inhibition of the LPL
727 pathway, granting tumor cells advantages in metabolism and immune evasion. Therefore,
728 maintaining or enhancing LPL function may have positive implications for mitigating the
729 hazards of environmental carcinogens. Taken together, the seemingly paradoxical roles of LPL
730 across cancers may reflect a context-dependent balance between its metabolic and
731 immunological functions. Understanding this balance is essential for accurately interpreting the
732 role of LPL in different tumor settings and may provide important insights for targeting lipid
733 metabolism in cancer therapy.

734 Importantly, recent advances in cancer therapy have highlighted the increasing importance of
735 immunotherapy and targeted treatment strategies in improving outcomes for patients with
736 advanced and metastatic malignancies. Novel immunotherapeutic approaches, including
737 engineered T-cell receptor (TCR)-based therapies and immune checkpoint-related strategies,
738 have been developed to enhance anti-tumor immune responses by improving antigen
739 recognition and T-cell activation (Zhao et al., 2021; Jin et al., 2019). However, tumor
740 heterogeneity and therapy resistance remain major challenges, particularly in metastatic
741 settings. Accumulating evidence suggests that the efficacy of immunotherapy is closely
742 associated with the tumor microenvironment (TME) and immune cell infiltration. Studies have
743 demonstrated that immune and stromal components within the TME are significantly correlated
744 with patient prognosis and therapeutic response, and that specific genes associated with
745 immune infiltration may serve as predictive biomarkers (Xiang et al., 2021). In particular, gene
746 expression patterns linked to immune cell abundance and tumor purity have been shown to
747 influence survival outcomes and may provide insight into immunotherapy responsiveness. In
748 addition, recent integrative analyses have identified immune-related functional genes as key
749 determinants of immunotherapy efficacy. For example, LCK has been reported to be highly
750 expressed in T cells and associated with increased tumor-infiltrating lymphocytes (TILs),

751 improved prognosis, and enhanced response to immunotherapy, highlighting the importance of
752 immune activation–related molecular markers (Wang et al., 2022). Furthermore, emerging
753 evidence indicates that epigenetic regulation, including noncoding RNA–mediated histone
754 modification, also contributes to tumor progression and may influence therapeutic sensitivity,
755 providing additional layers of molecular regulation (Yang et al., 2022). In this context, our
756 findings suggest that LPL, as a key regulator of lipid metabolism, may also play a role in
757 shaping the tumor immune microenvironment. Given its association with immune and stromal
758 infiltration observed in this study, LPL may function similarly to immune-related genes by
759 influencing immune cell behavior and tumor–immune interactions. Therefore, LPL may
760 represent a potential biomarker linking environmental exposure to tumor progression and
761 immunotherapy responsiveness, particularly in the context of metastatic HNSC.

762 DBP may promote tumorigenesis through multiple molecular pathways. Firstly, as an endocrine
763 disruptor, DBP can disrupt hormone receptor-mediated signaling pathways. For example,
764 reports indicate that DBP can weakly activate estrogen receptors or excessively activate nuclear
765 receptors such as peroxisome proliferator-activated receptors (PPARs), thereby altering
766 downstream gene expression and affecting cell proliferation and differentiation (Winz et al.,
767 2023; Wójtowicz et al., 2017). Secondly, DBP and other phthalates can activate the aryl
768 hydrocarbon receptor (AhR) pathway, a signaling axis known to be closely associated with
769 carcinogenesis induced by environmental pollutants. Activated AhR can trigger a series of pro-
770 carcinogenic signaling cascades, including promoting cell proliferation/anti-apoptosis,
771 inflammation, and metastasis. Literature shows that in breast cancer cells, low doses of
772 phthalates (such as DBP or analogs) can upregulate tumor-associated genes like histone
773 deacetylase 6 (HDAC6) and c-Myc via the AhR-PKA-CREB1 pathway, significantly
774 enhancing the proliferation, migration, and invasion capabilities of cancer cells (Hsieh et al.,
775 2012). Corresponding animal experiments have also demonstrated that long-term
776 administration of DBP to mice accelerates the growth of transplanted mammary tumors and
777 induces high expression of HDAC6 and c-Myc. Thirdly, DBP may promote malignant
778 progression processes such as epithelial-mesenchymal transition (EMT). From existing studies,
779 we know that phthalate exposure can lead to downregulation of E-cadherin and upregulation of

780 Vimentin and MMP2/9 in tumor cells; these changes in EMT markers are associated with
781 enhanced invasive and metastatic capabilities (Kim et al., 2023; Shih et al., 2024). In hepatoma
782 cell models, low-dose DBP can induce similar EMT changes and increase cancer cell stemness
783 via pathways such as AhR/ERK. In summary, DBP may promote the occurrence and
784 development of HNSC through endocrine disruption and AhR-mediated signaling
785 dysregulation, including enhancing tumor cell proliferation, survival, and invasion, as well as
786 inhibiting the body's immune surveillance.

787 In addition to these mechanisms, enrichment analysis and experimental data in this study
788 suggested a potential association between DBP exposure and PI3K–AKT–mTOR–related
789 signaling. However, pathway activation is primarily regulated at the level of protein
790 phosphorylation rather than transcriptional changes. Therefore, the observed upregulation of
791 PIK3CA, AKT1, and mTOR should be interpreted as transcriptional association rather than
792 definitive evidence of pathway activation. Notably, PI3K–AKT signaling can be modulated by
793 upstream post-translational mechanisms. For example, TRIM29 has been reported to promote
794 tumor progression by inducing ubiquitination-mediated degradation of NEFL, thereby relieving
795 its inhibitory effect on PI3K–AKT signaling and enhancing downstream pathway activity (Liu
796 et al., 2025). In the absence of protein-level validation, the involvement of this pathway in DBP-
797 mediated effects should be interpreted with caution.

798 DBP was used at 0, 0.1, 1, and 10 μ M in subsequent cell experiments. These concentrations
799 were selected according to previous in vitro toxicological studies showing that DBP exerts
800 measurable biological effects from nanomolar to micromolar ranges, together with our
801 preliminary cell viability testing. Because reported human circulating DBP levels are generally
802 lower, the selected concentrations should be interpreted as a mechanistically informative in
803 vitro exposure range rather than a direct simulation of physiological exposure (Wójtowicz et
804 al., 2017; Gutiérrez-García et al., 2024). Although DBP is detectable in human serum and blood,
805 the concentrations used in our in vitro experiments are higher than typical circulating exposure
806 levels reported in biomonitoring studies. Therefore, our findings mainly support the
807 mechanistic potential of DBP to modulate LPL expression and downstream signaling in HNSC
808 cells, rather than directly reproducing real-world internal exposure levels (Sicińska et al., 2020).

809 This study is the first to apply network toxicology to explore the association mechanism
810 between DBP and HNSC, identifying LPL as a potential key protective factor and validating it
811 through in vitro and in vivo experiments. This finding enriches our understanding of
812 environmental carcinogenic factors in HNSC. Previous HNSC research has focused more on
813 traditional carcinogens such as smoking and viruses, with insufficient attention paid to
814 environmental pollutants like DBP. The results of this study suggest that widely existing
815 endocrine disruptors in the environment should be incorporated into the research scope of the
816 etiology and prognosis of head and neck tumors. For instance, LPL has the potential to serve as
817 a protective biomarker for the body when exposed to environmental risk factors like DBP: we
818 observed that high LPL expression may reduce the risk of adverse outcomes in HNSC,
819 providing clues for future studies on the interaction between environmental exposure and
820 genetic susceptibility in populations. At the clinical and public health levels, our research
821 implies that reducing exposure to pollutants like DBP or enhancing the functional levels of
822 metabolic enzymes such as LPL in individuals may help lower the risk of head and neck
823 squamous cell carcinoma or improve patient prognosis. This inference awaits further in-depth
824 research, including epidemiological investigations with larger samples and validation of the
825 impact mechanism of the DBP-LPL axis on tumorigenesis in animal models.

826 Despite the integrative design of this study, several limitations should be acknowledged. First,
827 although we performed functional validation using SCC9 cells, all experimental evidence was
828 limited to in vitro assays. The absence of in vivo models restricts our ability to fully evaluate
829 the DBP-LPL axis within the complex tumor microenvironment. Second, this study relied
830 heavily on publicly available datasets, including TCGA and GEO. Although multiple
831 independent cohorts and analytical approaches were used to enhance robustness, potential batch
832 effects and data heterogeneity cannot be completely excluded. Third, most of our experimental
833 validation focused on mRNA expression levels, particularly for LPL and downstream signaling
834 molecules. The lack of protein-level validation limits the strength of mechanistic conclusions.
835 Finally, while molecular docking and dynamics simulations suggested stable binding between
836 DBP and LPL, the intracellular metabolism and bioactive forms of DBP were not investigated.
837 Therefore, the precise molecular interactions in a physiological context remain to be further

838 clarified. These limitations highlight the need for future studies incorporating in vivo validation,
839 proteomic analyses, and toxicokinetic investigations.

840 In addition, the interpretation of LPL expression patterns and their association with tumor stage
841 should be approached with caution. The transcriptomic analyses in this study were primarily
842 based on bulk datasets such as TCGA and GEO, which are inherently subject to both technical
843 and biological biases, including tumor heterogeneity, sample purity, and sequencing-related
844 variability (Liu et al., 2025, Liu et al., 2025). Furthermore, previous studies have emphasized
845 that elevated gene expression observed in cancer datasets does not necessarily imply a causal
846 role in tumor progression, and correlation-based findings should be interpreted carefully within
847 complex biological systems (Hengrui Liu et al., 2024). In particular, bulk RNA-seq data
848 represent averaged signals across heterogeneous cell populations and may obscure cell type-
849 specific expression patterns. This issue is especially relevant in the present study, as our
850 independent single-cell analyses indicate that LPL expression is predominantly enriched in non-
851 epithelial cell populations, including pericytes and stromal-associated cells. Therefore, the
852 observed associations between LPL expression and clinical features, including tumor stage,
853 may be influenced by variations in tumor microenvironment composition rather than solely
854 reflecting tumor cell-intrinsic regulation. In the absence of direct orthogonal validation in the
855 current study, we cannot exclude the possibility that these associations are at least partially
856 driven by stromal or immune cell components. Future studies incorporating approaches such as
857 immunohistochemistry or single-cell RNA sequencing will be necessary to further clarify the
858 cellular origin and functional relevance of LPL expression in HNSC.

859 In conclusion, this study, through a comprehensive strategy combining network toxicology,
860 molecular docking, and cellular experiments, has untangled the potential carcinogenic
861 pathways of DBP in head and neck squamous cell carcinoma, particularly its impact on
862 lipoprotein lipase (LPL) and the consequent metabolic and immune effects. We found that LPL
863 may play a protective role in DBP-associated HNSC progression, providing a new perspective
864 for elucidating the carcinogenic mechanisms of environmental endocrine disruptors. Our work
865 not only fills a gap in the research on environmental carcinogenic factors for HNSC but also
866 proposes the possibility of LPL as a potential intervention target. In the future, regulation

867 targeting the LPL pathway may become a new strategy for mitigating the hazards of
868 environmental carcinogens and synergizing with the prevention and treatment of head and neck
869 tumors. The novel findings of this study hold profound toxicological and molecular biological
870 significance for understanding the etiology of HNSC and formulating clinical and preventive
871 measures.

872

873 **CRedit authorship contribution statement**

874 **Guangming Li:** Writing – review & editing, Writing – original draft, Visualization,
875 Resources. **Yi Jin:** Writing – review & editing, Writing – original draft, Visualization. **Xiaowei**
876 **Yuan:** Writing – original draft, Visualization. **Xinyan Wu:** Visualization, Resources. **Long**
877 **Li:** Writing – review & editing, Writing – original draft. **Jiashu Liao:** Writing – review &
878 editing, Visualization, Methodology. **Shanshan Cai:** Writing – review & editing, Resources,
879 Methodology, Formal analysis.

880

881 **Funding**

882 This research did not receive any specific grant from funding agencies in the public, commercial,
883 or not-for-profit sectors.

884

885 **Declaration of competing interest**

886 The authors declare that they have no known competing financial interests or personal
887 relationships that could have appeared to influence the work reported in this paper.

888

889 **References**

890 1. F. Arrigo, F. Impellitteri, G. Piccione, C. Faggio Phthalates and their effects on human
891 health: focus on erythrocytes and the reproductive system. Comparative biochemistry

- 892 and physiology Toxicol. Pharmacol.: CBP, 270 (2023),
893 Article 109645, 10.1016/j.cbpc.2023.109645
- 894 2. A. Báez Genetic and environmental factors in head and neck cancer genesis J. Environ.
895 Sci. Health C Environ. Carcinog. Ecotoxicol. Rev., 26 (2) (2008), pp. 174-
896 200, 10.1080/10590500802129431
- 897 3. A. Barsouk, J.S. Aluru, P. Rawla, K. Saginala, A. Barsouk Epidemiology, risk factors,
898 and prevention of head and neck squamous cell carcinoma Med. Sci., 11 (2) (2023),
899 p. 42, 10.3390/medsci11020042
- 900 4. L. Berglund, E. Björling, P. Oksvold, *et al.* A gene-centric human protein atlas for
901 expression profiles based on antibodies Mol. Cell. Proteomics, 7 (10) (2008), pp. 2019-
902 2027, 10.1074/mcp.R800013-MCP200
- 903 5. H.M. Berman, J. Westbrook, Z. Feng, *et al.* The protein data bank Nucleic Acids
904 Res., 28 (1) (2000), pp. 235-242, 10.1093/nar/28.1.235
- 905 6. J. Borén, M.R. Taskinen, E. Björnson, C.J. Packard Metabolism of triglyceride-rich
906 lipoproteins in health and dyslipidaemia Nat. Rev. Cardiol., 19 (9) (2022), pp. 577-
907 592, 10.1038/s41569-022-00676-y
- 908 7. M. Cannon, J. Stevenson, K. Stahl, *et al.* DGIdb 5.0: rebuilding the drug-gene
909 interaction database for precision medicine and drug discovery platforms Nucleic
910 Acids Res., 52 (D1) (2024), pp. D1227-D1235, 10.1093/nar/gkad1040
- 911 8. E. Cerami, J. Gao, U. Dogrusoz, *et al.* The cBio cancer genomics portal: an open
912 platform for exploring multidimensional cancer genomics data Cancer
913 Discov., 2 (2012), pp. 401-404, 10.1158/2159-8290.CD-12-0095
- 914 9. D. Cerne, E. Melkic, Z. Trost, M. Sok, J. Marc Lipoprotein lipase activity and gene
915 expression in lung cancer and in adjacent noncancer lung tissue Exp. Lung
916 Res., 33 (5) (2007), pp. 217-225, 10.1080/01902140701481054
- 917 10. CNCB-NGDC Members and Partners Database resources of the national genomics data

- 918 center, China National Center for bioinformation in 2024 *Nucleic Acids*
919 *Res.*, 52 (D1) (2024), pp. D18-D32, 10.1093/nar/gkad1078
- 920 11. CNCB-NGDC Members and Partners Database resources of the national genomics data
921 center, China national center for bioinformation in 2025 *Nucleic Acids*
922 *Res.*, 53 (D1) (2025), pp. D30-D44, 10.1093/nar/gkae978
- 923 12. CNCB-NGDC Members and Partners. Database resources of the National Genomics
924 Data Center China national center for bioinformation *Nucleic Acids*
925 *Res.*, 50 (D1) (2022), pp. D27-D38, 10.1093/nar/gkab951
- 926 13. H. Cui, G. Zhao, Y. Lu, S. Zuo, D. Duan, X. Luo, H. Zhao, J. Li, Z. Zeng, Q. Chen, T.
927 Li *TIMER3*: an enhanced resource for tumor immune analysis *Nucleic Acids*
928 *Res.*, 53 (W1) (2025), pp. W534-W541, 10.1093/nar/gkaf388
- 929 14. A.P. Davis, C.G. Murphy, C.A. Saraceni-Richards, *et al.* Comparative toxicogenomics
930 database: a knowledgebase and discovery tool for chemical-gene-disease networks
931 *Nucleic Acids Res.*, 37 (D1) (2009), pp. D786-D792, 10.1093/nar/gkn580
- 932 15. A.P. Davis, T.C. Wieggers, R.J. Johnson, *et al.* Comparative Toxicogenomics Database
933 (CTD): update 2023 *Nucleic Acids Res.*, 51 (D1) (2023), pp. D1257-
934 D1262, 10.1093/nar/gkac833
- 935 16. I. de Bruijn, R. Kundra, B. Mastrogiacomo, *et al.* Analysis and visualization of
936 longitudinal genomic and clinical data from the AACR project GENIE biopharma
937 collaborative in cBioPortal *Cancer Res.*, 83 (23) (2023), pp. 3861-
938 3867, 10.1158/0008-5472.CAN-23-0816
- 939 17. W. Fu, A. Sun, H. Dai Lipid metabolism involved in progression and drug resistance
940 of breast cancer *Genes Dis.*, 12 (4) (2024),
941 Article 101376, 10.1016/j.gendis.2024.101376
- 942 18. J. Gao, B.A. Aksoy, U. Dogrusoz, *et al.* Integrative analysis of complex cancer
943 genomics and clinical profiles using the cBioPortal *Sci.*
944 *Signal.*, 6 (269) (2013), 10.1126/scisignal.2004088

- 945 19. M. Gormley, G. Creaney, A. Schache, K. Ingarfield, D.I. Conway Reviewing the
946 epidemiology of head and neck cancer: definitions, trends and risk factors *Br. Dent.*
947 *J.*, 233 (9) (2022), pp. 780-786, 10.1038/s41415-022-5166-x
- 948 20. A.K. Gutiérrez-García, D.A. Torres-García, A. De Leon-Rodriguez Diethyl phthalate
949 and dibutyl phthalate disrupt sirtuins expression in the HepG2 cells *Toxicol.*
950 *Res.*, 13 (4) (2024), 10.1093/toxres/tfae103
- 951 21. Z. Hengrui Liu, Z. Guo, P. Wang Genetic expression in cancer research: challenges and
952 complexity *Gene Rep.*, 37 (2024), Article 102042, 10.1016/j.genrep.2024.102042
- 953 22. T.H. Hsieh, C.F. Tsai, C.Y. Hsu, P.L. Kuo, J.N. Lee, C.Y. Chai, S.C. Wang, E.M. Tsai
954 Phthalates induce proliferation and invasiveness of estrogen receptor-negative breast
955 cancer through the AhR/HDAC6/c-Myc signaling pathway *FASEB J. : Off. Publ. Feder.*
956 *Am. Soc. Exp. Biol.*, 26 (2) (2012), pp. 778-787, 10.1096/fj.11-191742
- 957 23. J. Jin, X. Wu, J. Yin, M. Li, J. Shen, J. Li, Y. Zhao, Q. Zhao, J. Wu, Q. Wen, C.H. Ch
958 o, T. Yi, Z. Xiao, L. Qu Identification of genetic mutations in cancer: challenge and
959 opportunity in the new era of targeted therapy *Front. Oncol.*, 9 (2019),
960 p. 263, 10.3389/fonc.2019.00263
- 961 24. H.R. Jin, J. Wang, Z.J. Wang, M.J. Xi, B.H. Xia, K. Deng, J.L. Yang Lipid metabolic
962 reprogramming in tumor microenvironment: from mechanisms to therapeutics *J.*
963 *Hematol. Oncol.*, 16 (1) (2023), p. 103, 10.1186/s13045-023-01498-2
- 964 25. D.E. Johnson, B. Burtness, C.R. Leemans, V.W.Y. Lui, J.E. Bauman, J.R. Grandis
965 Head and neck squamous cell carcinoma *Nat. Rev. Dis. Primers*, 6 (1) (2020),
966 p. 92, 10.1038/s41572-020-00224-3
- 967 26. S. Kersten Physiological regulation of lipoprotein lipase *Biochim. Biophys.*
968 *Acta*, 1841 (7) (2014), pp. 919-933, 10.1016/j.bbalip.2014.03.013
- 969 27. J.H. Kim Di(2-ethylhexyl) phthalate promotes lung cancer cell line A549 progression
970 via Wnt/ β -catenin signaling *J. Toxicol. Sci.*, 44 (4) (2019), pp. 237-
971 244, 10.2131/jts.44.237

- 972 28. S. Kim, J. Chen, T. Cheng, *et al.* PubChem 2023 update Nucleic Acids
973 Res., 51 (D1) (2023), pp. D1373-D1380, 10.1093/nar/gkac956
- 974 29. B. Li, E. Severson, J.C. Pignon, *et al.* Comprehensive analyses of tumor immunity:
975 implications for cancer immunotherapy Genome Biol., 17 (2016),
976 p. 174, 10.1186/s13059-016-1028-7
- 977 30. T. Li, J. Fan, B. Wang, N. Traugh, Q. Chen, J.S. Liu, B. Li, X.S. Liu TIMER: a web
978 server for comprehensive analysis of tumor-infiltrating immune cells Cancer
979 Res., 77 (21) (2017), pp. e108-e110, 10.1158/0008-5472.CAN-17-0307
- 980 31. T. Li, J. Fu, Z. Zeng, *et al.* TIMER2.0 for analysis of tumor-infiltrating immune cells
981 Nucleic Acids Res., 48 (W1) (2020), pp. W509-W514, 10.1093/nar/gkaa407
- 982 32. M. Li, X. Zhang, K.S. Ang, *et al.* DISCO: a database of deeply integrated human
983 single-cell omics data Nucleic Acids Res., 50 (D1) (2022), pp. D596-
984 D602, 10.1093/nar/gkab1020
- 985 33. L. Li, L. Huang, R. Lei, P. Zhang, Y. Yang, H. Liu, Y. Zhang DEHP and DBP,
986 common phthalates, induce glucose metabolism disorders in rats via oxidative damage
987 of PI3K/Akt/GLUT4 signaling Environ. Pollut., 341 (2024),
988 Article 122948, 10.1016/j.envpol.2023.122948
- 989 34. M. Li, K.S. Ang, B. Teo, *et al.* Rediscovering publicly available single-cell data with
990 the DISCO platform Nucleic Acids Res., 53 (D1) (2025), pp. D932-
991 D938, 10.1093/nar/gkae1108
- 992 35. Y. Liu, N. Zhang, Y. Wen, J. Wen Head and neck cancer: pathogenesis and targeted
993 therapy MedComm, 5 (9) (2024), Article e702, 10.1002/mco2.702
- 994 36. H. Liu, Y. Li, M. Karsidag, T. Tu, P. Wang Technical and biological biases in bulk
995 transcriptomic data mining for cancer research J. Cancer, 16 (1) (2025), pp. 34-
996 43, 10.7150/jca.100922
- 997 37. Y. Liu, Q. He, L. Zhu, M. Zhong, H. Zhuang, N. Zhao, Y. Cai, C. Cheng, J. Shao

- 998 TRIM29 promotes glioblastoma progression via ubiquitinating NEFL and activating
999 the PI3K/AKT signaling pathway *Cancer Genet.*, 296–297 (2025), pp. 88-
1000 99, 10.1016/j.cancergen.2025.06.008
- 1001 38. J. Lv, S. Sun, R. Wu, X. Li, Y. Bai, J. Xu, C. Guo Phthalate esters in dusts from
1002 different indoor and outdoor microenvironment and potential human health risk: a case
1003 study in Beijing *Environ. Res.*, 266 (2025),
1004 Article 120513, 10.1016/j.envres.2024.120513
- 1005 39. Q. Ma, R. Kang, R. Xu, Y. Guan, S. Chang, S. Li Crosstalk between stromal, immune,
1006 and ovarian cancer cells in lipid-rich tumor microenvironment exhibits proliferative
1007 features *Front. Immunol.*, 16 (2025), Article 1614815, 10.3389/fimmu.2025.1614815
- 1008 [View in Scopus](#)[Google Scholar](#)
- 1009 40. C.J. Mattingly, M.C. Rosenstein, A.P. Davis, G.T. Colby, J.N. Forrest Jr., J.L. Boyer
1010 The comparative toxicogenomics database: a cross-species resource for building
1011 chemical-gene interaction networks *Toxicol. Sci.*, 92 (2) (2006), pp. 587-
1012 595, 10.1093/toxsci/kfl008
- 1013 41. M. Meng, Y. Yang, L. Song, J. Peng, S. Li, Z. Gao, Y. Bu, J. Gao Association between
1014 urinary phthalates and phthalate metabolites and cancer risk: a systematic review and
1015 meta-analysis *Heliyon*, 10 (8) (2024), Article e29684, 10.1016/j.heliyon.2024.e29684
- 1016 42. B. Oliviero, A. Caretti, M.U. Mondelli, S. Mantovani Lipid metabolism
1017 reprogramming in tumor-associated macrophages modulates their function in primary
1018 liver cancers *Cancers*, 17 (11) (2025), p. 1858, 10.3390/cancers17111858
- 1019 43. J. Pan, P. Liu, X. Yu, Z. Zhang, J. Liu The adverse role of endocrine disrupting
1020 chemicals in the reproductive system *Front. Endocrinol.*, 14 (2024),
1021 Article 1324993, 10.3389/fendo.2023.1324993
- 1022 44. J.O. Park, Y.M. Park, W.J. Jeong, Y.S. Shin, Y.T. Hong, *et al.* Survival benefits from
1023 surgery for stage IVa head and neck squamous cell carcinoma: a multi-institutional
1024 analysis of 1,033 cases *Clin. Exp. Otorhinolaryngol.*, 14 (2) (2021), pp. 225-

- 1025 234, 10.21053/ceo.2020.01732
- 1026 45. M.S. Shih, F.M. Suk, W.C. Chiu, C.Y. Lee, F.Y. Hsu, Y.J. Liao Long-term di-(2-
1027 ethylhexyl) phthalate exposure reduces sorafenib treatment efficacy by enhancing
1028 mesenchymal transition in hepatocellular carcinoma *Ecotoxicol. Environ.*
1029 *Saf.*, 273 (2024), Article 116161, 10.1016/j.ecoenv.2024.116161
- 1030 46. P. Sicińska, K. Kik, B. Bukowski Human erythrocytes exposed to phthalates and their
1031 metabolites alter antioxidant enzyme activity and hemoglobin oxidation *Int. J. Mol.*
1032 *Sci.*, 21 (12) (2020), p. 4480, 10.3390/ijms21124480
- 1033 47. V. Silano, J.M. Barat Baviera, C. Bolognesi, A. Chesson, P.S. Cocconcelli, EFSA
1034 Panel on Food Contact Materials, Enzymes and Processing Aids (CEP) Update of the
1035 risk assessment of di-butylphthalate (DBP), butyl-benzyl-phthalate (BBP), bis(2-
1036 ethylhexyl)phthalate (DEHP), di-isononylphthalate (DINP) and di-isodecylphthalate
1037 (DIDP) for use in food contact materials *EFSA J. European Food Safety*
1038 *Authority*, 17 (12) (2019), Article e05838,
- 1039 48. D. Sonkin, A. Thomas, B.A. Teicher Cancer treatments: past, present, and future
1040 *Cancer Genet.*, 286–287 (2024), pp. 18-24, 10.1016/j.cancergen.2024.06.002
- 1041 49. Z. Trost, M. Sok, J. Marc, D. Cerne Increased lipoprotein lipase activity in non-small
1042 cell lung cancer tissue predicts shorter patient survival *Arch. Med. Res.*, 40 (5) (2009),
1043 pp. 364-368, 10.1016/j.arcmed.2009.05.001
- 1044 50. S. Ubaid, R. Kushwaha, M. Kashif, V. Singh Comprehensive analysis of oncogenic
1045 determinants across tumor types via multi-omics integration *Cancer Genet.*, 298–
1046 299 (2025), pp. 44-62, 10.1016/j.cancergen.2025.08.010
- 1047 51. M. Uhlén, C. Zhang, S. Lee, *et al.* A pathology atlas of the human cancer transcriptome
1048 *Science*, 357 (6352) (2017), 10.1126/science.aan2507
- 1049 52. . Wang, J. Xiao, T.O. Suzek, *et al.* PubChem's BioAssay database *Nucleic Acids*
1050 *Res.*, 40 (D1) (2012), pp. D400-D412, 10.1093/nar/gkr1132

- 1051 53. F. Wang, A. Zheng, D. Zhang, T. Zou, M. Xiao, J. Chen, B. Wen, Q. Wen, X. Wu, M.
1052 Li, F. Du, Y. Chen, Y. Zhao, J. Shen, S. Xiang, J. Li, S. Deng, Z. Zhang, T. Yi, Z. Xia
1053 o Molecular profiling of core immune-escape genes highlights LCK as an immune-
1054 related prognostic biomarker in melanoma *Front. Immunol.*, 13 (2022),
1055 Article 1024931, 10.3389/fimmu.2022.1024931
- 1056 54. J. Wang, H. Guo, L.F. Zheng, P. Li, T.J. Zhao Context-specific fatty acid uptake is a
1057 finely-tuned multi-level effort *Trends Endocrinol. Metabol.: TEM (Trends Endocrinol.*
1058 *Metab.)*, 36 (6) (2025), pp. 577-590, 10.1016/j.tem.2024.10.001
- 1059 55. C. Winz, W.X. Zong, N. Suh Endocrine-disrupting compounds and metabolomic
1060 reprogramming in breast cancer *J. Biochem. Mol. Toxicol.*, 37 (12) (2023),
1061 Article e23506, 10.1002/jbt.23506
- 1062 56. A.K. Wójtowicz, K.A. Szychowski, A. Wnuk, M. Kajta Dibutyl phthalate (DBP)-
1063 induced apoptosis and neurotoxicity are mediated via the Aryl hydrocarbon Receptor
1064 (AhR) but not by estrogen Receptor alpha (ER α), Estrogen Receptor beta (ER β), or
1065 peroxisome proliferator-activated receptor gamma (PPAR γ) in mouse cortical neurons
1066 *Neurotox. Res.*, 31 (1) (2017), pp. 77-89, 10.1007/s12640-016-9665-x
- 1067 57. S. Xiang, J. Li, J. Shen, Y. Zhao, X. Wu, M. Li, X. Yang, P.J. Kaboli, F. Du, Y. Zheng,
1068 Q. Wen, C.H. Cho, T. Yi, Z. Xiao Identification of prognostic genes in the tumor
1069 microenvironment of hepatocellular carcinoma *Front. Immunol.*, 12 (2021),
1070 Article 653836, 10.3389/fimmu.2021.653836
- 1071 58. T. Xiang, J. Liu, X. Yang, D. Zhang, Q. Shen, X.C. Le, X.F. Li Disinfection
1072 byproducts confirmed over 50 years: systematic curation, modes of toxic action, and
1073 toxicogenomics *Environ. Sci. Technol.*, 59 (42) (2025), pp. 22334-
1074 22350, 10.1021/acs.est.4c13900
- 1075 59. J. Xiao, S. Cao, J. Wang, P. Li, Q. Cheng, X. Zhou, J. Dong, Y. Li, X. Zhao, Z. Xu, L.
1076 Yang Leptin-mediated suppression of lipoprotein lipase cleavage enhances lipid
1077 uptake and facilitates lymph node metastasis in gastric cancer *Cancer*
1078 *Commun.*, 44 (8) (2024), pp. 855-878, 10.1002/cac2.12583

- 1079 60. Q. Yang, Y. Chen, R. Guo, Y. Dai, L. Tang, Y. Zhao, X. Wu, M. Li, F. Du, J. Shen, T.
1080 Yi, Z. Xiao, Q. Wen Interaction of ncRNA and epigenetic modifications in gastric
1081 cancer: focus on histone modification *Front. Oncol.*, 11 (2022),
1082 Article 822745, 10.3389/fonc.2021.822745
- 1083 61. K. Yang, X. Wang, C. Song, Z. He, R. Wang, Y. Xu, G. Jiang, Y. Wan, J. Mei, W. Ma
1084 o The role of lipid metabolic reprogramming in tumor microenvironment
1085 *Theranostics*, 13 (6) (2023), pp. 1774-1808, 10.7150/thno.82920
- 1086 62. L. Yang, X. Fang, X. Liu, Y. Liu, S. Zhao Lipid metabolism-associated immune gene
1087 LPL promotes M1 macrophage polarization and inhibits breast cancer progression
1088 *Tissue Cell*, 97 (2025), Article 103071, 10.1016/j.tice.2025.103071
- 1089 63. Y. Yu, J.Q. Wang Phthalate exposure and lung disease: the epidemiological evidences,
1090 plausible mechanism and advocacy of interventions *Rev. Environ.*
1091 *Health*, 39 (1) (2022), pp. 37-45, 10.1515/reveh-2022-0077
- 1092 64. N. Zaidi, L. Lupien, N.B. Kuemmerle, W.B. Kinlaw, J.V. Swinnen, K. Smans
1093 Lipogenesis and lipolysis: the pathways exploited by the cancer cells to acquire fatty
1094 acids *Prog. Lipid Res.*, 52 (4) (2013), pp. 585-589, 10.1016/j.plipres.2013.08.005
- 1095 65. Q. Zhao, Y. Jiang, S. Xiang, P.J. Kaboli, J. Shen, Y. Zhao, X. Wu, F. Du, M. Li, C.H.
1096 Cho, J. Li, Q. Wen, T. Liu, T. Yi, Z. Xiao Engineered TCR-T cell immunotherapy in
1097 anticancer precision medicine: pros and cons *Front. Immunol.*, 12 (2021),
1098 Article 658753, 10.3389/fimmu.2021.658753
- 1099
1100